Identification and characterization of intermediate states in mammalian neural crest cell epithelial to mesenchymal transition and delamination

Ruonan Zhao[1,2], Emma L. Moore[1], Madelaine M Gogol[1], Jay R. Uhruh[1], Zulin Yu[1], Allison Scott[1], Yan Wang [1], Naresh Kumar Rajendran[1] and Paul A. Trainor[1,2*]

[1]Stowers Institute for Medical Research, Kansas City, MO, USA

[2]Department of Anatomy and Cell Biology, University of Kansas Medical Center, Kansas City, KS, USA

*Author for Correspondence: pat@stowers.org

Keywords: neural crest cells; epithelial to mesenchymal transition; EMT; epithelial to mesenchymal plasticity; EMP; mouse; cell cycle; Dlc1

Abstract

Epithelial to mesenchymal transition (EMT) is a cellular process that converts epithelial cells to mesenchymal cells with migratory potential in both developmental and pathological processes. Although originally considered a binary event, EMT in cancer progression involves intermediate states between a fully epithelial and a fully mesenchymal phenotype, which are characterized by distinct combinations of epithelial and mesenchymal markers. This phenomenon has been termed epithelial to mesenchymal plasticity (EMP), however, the intermediate states remain poorly described and it's unclear whether they exist during developmental EMT. Neural crest cells (NCC) are an embryonic progenitor cell population that gives rise to numerous cell types and tissues in vertebrates, and their formation is a classic example of developmental EMT. An important feature of NCC development is their delamination from the neuroepithelium via EMT, following which NCC migrate throughout the embryo and undergo differentiation. NCC delamination shares similar changes in cellular state and structure with cancer cell invasion. However, whether intermediate states also exist during NCC EMT and delamination remains unknown. Through single cell RNA sequencing, we identified intermediate NCC states based on their transcriptional signature and then spatially defined their locations in situ in the dorsolateral neuroepithelium. Our results illustrate the progressive transcriptional and spatial transitions from premigratory to migratory cranial NCC during EMT and delamination. Of note gene expression and trajectory analysis indicate that distinct intermediate populations of NCC delaminate in either S phase or G2/M phase of the cell cycle, and the importance of cell cycle regulation in facilitating mammalian cranial NCC delamination was confirmed through cell cycle inhibition studies. Additionally, transcriptional knockdown revealed a functional role for the intermediate stage marker *Dlc1* in regulating NCC delamination and migration. Overall, our work identifying and characterizing the intermediate cellular states, processes, and molecular signals that regulate mammalian NCC EMT and delamination furthers our understanding of developmental EMP and may provide new insights into mechanisms regulating pathological EMP.

Introduction

Epithelial to mesenchymal transition (EMT) is a cellular process that converts epithelial cells to mesenchymal cells with migratory potential (Hay 1995). EMT plays an essential role in various developmental and pathological processes such as embryonic morphogenesis, wound healing, tissue fibrosis and cancer progression (Zhao and Trainor 2023). Studies of EMT, particularly in the field of cancer biology, have increased exponentially in the past 5 years due to the implied role of EMT in numerous aspects of malignancy such as cancer cell invasion, survival, stemness, metastasis, therapeutic resistance and tumor heterogeneity (Yang et al. 2020a).

EMT has traditionally been considered a binary process comprising either full epithelial cell or mesenchymal cell states. However, studies of cancer have uncovered an alternative scenario termed epithelial to mesenchymal plasticity (EMP), in which multiple intermediate states exist along the EMT spectrum (Dong et al. 2018; Gonzalez et al. 2018; Huang et al. 2013; Karacosta et al. 2019; Kumar et al. 2019; Pastushenko et al. 2018). More specifically, in some cases of head and neck cancer, primary tumors and matching lymph nodes contain a subpopulation of tumor cells in a partial EMT state, as defined by their expression of both epithelial marker genes and mesenchymal marker genes (Puram et al. 2017). Moreover, cells in this partial EMT state are highly invasive and located at the leading edge of tumors *in vivo*. Similarly, in mouse xenograft models of skin cancer and breast cancer, the absence of epithelial cellular adhesion molecules in several cell populations was discovered to represent early EMT hybrid states as they also expressed both Vimentin and Cytokeratin 14 at intermediate levels and consequently had high metastatic potential (Pastushenko et al. 2018). Partial EMT states have also been recognized in lung cancer and ovarian cancer (Gonzalez et al. 2018; Karacosta et al. 2019), with tumor cells expressing both the epithelial marker E-cadherin, and the mesenchymal marker Vimentin. Besides primary tumors, EMT intermediate states have also been identified in circulating tumor cells from patient samples (Yu et al. 2013). Even though EMT intermediate states have been discovered in numerous studies, few have focused on describing and understanding the molecular and cellular mechanisms governing or defining each intermediate state due to the challenges of studying cancer initiation and progression *in vivo*.

Since EMT during embryogenesis and cancer progression have been shown to share analogous phenotypic changes that involve similar core transcription factors and molecular mechanisms, it was proposed that the initiation and development of carcinoma could be attributed to an unusual activation of EMT factors involved in normal developmental processes (Hay 1995). However, compared to tumorigenesis, it remains largely unknown whether intermediate or transition states exist or play a role in classic developmental EMT. Therefore, identifying and characterizing intermediate states during developmental EMT can further our understanding of the cellular processes, and molecular signaling networks that regulate EMP.

NCC formation is a classic example of developmental EMT (Lee et al. 2013; Zhao and Trainor 2023). NCC are a migratory progenitor cell population unique to vertebrates. Formed during neurulation in the dorsolateral domain of the neural plate, EMT facilitates their delamination from the neuroepithelium and migration throughout the body, where they differentiate into neurons and glia of the peripheral nervous system, pigment cells in the skin,

craniofacial bone and cartilage, as well as many other cell types (Bhatt et al. 2013; Dash and Trainor 2020; Lièvre and Douarin 1975; Trainor 2005; Weston 1983). Disruption of NCC delamination and migration can result in developmental abnormalities, referred to as neurocristopathies (Achilleos and Trainor 2015; Watt and Trainor 2014), hence it is important to study the mechanisms that regulate mammalian NCC development.

We performed single cell RNA sequencing (scRNA-seq) to identify and define intermediate transcriptional and cellular states during mouse cranial NCC EMT and delamination. We identified two NCC EMT intermediate populations distinguished by their S or G2/M cell cycle phase state during delamination. Interestingly, trajectory analyses reveal that these distinct intermediate populations are formed simultaneously, and independently, but then converge into a single or common pool, suggesting they do not have distinct fates following migration. This is consistent with the known plasticity and potency of early migrating NCC (Golding et al. 2000; Sandell and Trainor 2006; Trainor and Krumlauf 2000a; Trainor and Krumlauf 2000b, 2001). Transcriptional profiling revealed that the intermediate NCC populations could also be defined by unique transcriptional signatures, including differential expression of genes involved in cell protrusion, such as *Dlc1*, *Pak3* and *Sp5*. Further interrogation using SABER-FISH, revealed that these intermediate NCC populations were spatially localized in the dorsolateral region of the neural plate. In addition, knocking down the NCC EMT intermediate marker *Dlc1* led to a significant reduction in the number of migratory NCC, which revealed a critical role for *Dlc1* in the regulation of mouse cranial NCC delamination. Overall, our findings provide novel, detailed, high-resolution descriptions of the intermediate cell populations, and transcriptional states that occur during cranial NCC EMT and delamination in mouse embryos. Our work further illustrates that molecular characterization of NCC EMT intermediate states can reveal essential regulatory components of mouse NCC EMT and delamination. These results shed light on similar mechanisms of NCC EMT and delamination in other mammalian species as well and will also serve as a resource for the community. In addition to furthering our understanding of the cellular processes, and molecular signaling networks that regulate NCC and EMT delamination, our work may also help to inform the phenotypic changes and corresponding gene regulatory control of EMP in other developmental EMT events as well as pathological conditions such as tissue fibrosis and cancer progression.

Results

Identification of intermediate stages during mouse cranial NCC EMT and delamination

To investigate the biological process and mechanisms governing mouse cranial NCC EMT and delamination, we performed scRNA-seq on dissociated cranial tissues isolated from E8.5 mouse embryos with 7-9 somites (Figure 1A). More specifically, embryos were collected from two transgenic mouse lines: *Wnt1-Cre;RosaeYFP* (Chai et al. 2000) and *Mef2c-F10N-LacZ* (Aoto et al. 2015) (Figure 1A). In E8.5 *Wnt1-Cre;RosaeYFP* embryos, YFP is expressed by *Wnt1+* neuroepithelial cells located in the dorsolateral neural plate, which encompasses premigratory NCC (Figure 1B). Consequently, *Wnt1-Cre;RosaeYFP* labels premigratory and migratory NCC and other lineage labeled cells derived from the *Wnt1+* cell population (Figure 1B) (Chai et al. 2000). In contrast, *Mef2c-F10N-LacZ* predominantly labels migratory NCC, with lacZ activity driven by

the F10N enhancer of the *Mef2C* gene (Figure 1B) (Aoto et al. 2015). The two different transgenic lines allowed us to distinguish premigratory from migratory NCC spatially within an embryo, but also later bioinformatically following single cell dissociation and RNA-sequencing.

The scRNA-seq data was processed and analyzed as previously described (Falcon et al. 2022). We initially identified 6 major cell or tissue types present in E8.5 mouse embryonic cranial tissues based on the differential expression of classic cell or tissue type specific markers, and we clustered the data accordingly (Figure 1C and 1D; Figure 1-figure supplement 1). For example, *Sox1* and *Sox2* were used to delineate neural ectoderm, whereas *Cdh1* (E-cadherin) was used to define non-neural ectoderm. *eYFP*, *lacZ*, *Sox10* and *Twist* delineated migrating neural crest cells. *Tbx1* was primarily used as a marker of mesoderm cells and *Kdr* (*Vegfr2*) demarcated mesoderm-derived endothelial cells. We then bioinformatically segregated the cranial NCC cluster, which includes both premigratory and migratory NCC, and divided it into 5 subclusters at a resolution of 0.26 (Figure 2A).

To characterize these NCC subclusters, we then interrogated the expression of known neuroepithelial and neural plate border markers, as well as genes expressed by NCC during their specification and migration (Supplementary Table 1) (Echelard et al. 1994; Hafemeister and Satija 2019; Lee et al. 2013; Murdoch et al. 2012; Parr et al. 1993; Sauka-Spengler and Bronner-Fraser 2008; Wood and Episkopou 1999). A high percentage of cells in subclusters 0-3 express elevated levels of markers of migratory NCC (*Vim*, *Sox10*, *Twist1*), while only subclusters 0 and 1 exhibit high levels of expression of NCC specifier genes (*Zeb2*, *Pax3*, *Nr6a1*, *Sox9*, *Foxd3*, *Snai1)* (Figure 2B) (Cheung et al. 2005; Dottori et al. 2001; Hari et al. 2012; Kobayashi et al. 2020; Lee et al. 2013; Li et al. 2000; Murdoch et al. 2012; Schorle et al. 1996; Soo et al. 2002; Van de Putte et al. 2003). Since NCC specifiers are downregulated as NCC migrate and later differentiate into specific lineages, the combinatorial expression of genes suggests that subclusters 0 and 1 likely represent an earlier stage of NCC delamination and migration than subclusters 2 and 3. This conclusion was further verified by integrating previously published networks of genes that represent an early migratory NCC program versus a late migratory NCC program (Soldatov et al. 2019). Early migratory NCC program genes are expressed by the majority of migratory NCC whereas late migratory NCC program genes are only expressed in a subset of migratory NCC as they have already begun to mature.

Subclusters 0-3 each exhibits significant expression of early migratory NCC program genes (Figure 2-figure supplement 1). Furthermore, subclusters 2 and 3 express a significantly higher level of late migratory NCC program genes than subclusters 0 and 1, which demonstrates that subclusters 0 and 1 contain early migratory NCC, whereas subclusters 2 and 3 comprise late migratory NCC (Figure 2-figure supplement 1). Interestingly, we also observed that a small percentage of subcluster 0 cells express early migratory NCC genes, but at a lower intensity compared to subcluster 1. This implies that subcluster 0 might also contain premigratory NCC that do not yet express any migratory NCC genes (Figure 2-figure supplement 1). Despite similar expression profiles, NCC subclusters 2 and 3 possibly represent undifferentiated NCC derived mesenchyme tissue in different parts of the head. More specifically, subcluster 2 displays a high level of expression of pharyngeal arch NCC mesenchyme marker *Dlx2* (Figure 2-figure supplement 1) (Bulfone et al. 1993). In contrast, subcluster 3 expresses a frontonasal mesenchyme marker *Alx1* (Figure 2-figure supplement 1) (Iyyanar et al. 2022). Consistent with these observations, neither population expresses a high level of neurogenic lineage markers

such as *Nrp1* and Nrp2, which is indicative of their undifferentiated state (Figure 2-figure supplement 1) (Lumb et al. 2014).

Subcluster 4 exhibits a unique transcriptional profile distinct from subclusters 0-3 (Figure 2B). Higher expression of *Sox1* and *Sox2* is indicative of a neuroepithelial identity for subcluster 4 (Figure 2B). During NCC formation, Sox1 and Sox2 activity are downregulated in the dorsal neural plate border domain but remain strongly expressed more ventrally throughout the neural plate (Supplementary Table 1). Concomitantly, Sox9 and Sox10 are activated in what is known as the SoxB (1/2) to SoxE (9/10) switch (Mandalos et al. 2014; Remboutsika et al. 2011; Wakamatsu et al. 2004). Consistent with this model, overexpressing *Sox2* in the dorsal neural tube has been shown to repress NCC specification, whereas overexpressing *Sox9* and *Sox10* have been shown to precociously promote NCC formation (Aybar et al. 2003; Cheung and Briscoe 2003; Mandalos et al. 2014; McKeown et al. 2005; Remboutsika et al. 2011).

To determine if mouse cranial NCC EMT is non-binary, and occurs through intermediate or transition states, we further subdivided the 5 cranial NCC clusters into smaller subclusters (resolution=2.0; subcluster 1'-21') and extracted 15 subclusters out of the original early migratory NCC subclusters 0, 1 and 4 (Figure 2C; Figure 2-figure supplement 1). Through heatmap analysis, expression of the same NCC marker genes as described above was examined within these new subclusters, and the order of the subclusters was arranged according to their combinatorial expression patterns (Figure 2D). For example, *Wnt1* and *Sox10* were used to identify NCC transitioning from premigratory to migratory states since *Wnt1* is only expressed in premigratory NCC and is immediately downregulated as NCC delaminate and start to migrate. In contrast, *Sox10* is activated only after NCC have delaminated and begun to migrate. The heatmap shows that a significant number of cells in subcluster 17' express a much higher level of *Wnt1* than any other subcluster, suggesting that subcluster 17' comprises premigratory NCC (Figure 2D). Consistent with this observation, subcluster 17' cells also express other neural plate border and NCC specifier genes such as *Zic2*, *Pax7*, *Nr6a1*, *Pax3*, *Sox9*, and *Foxd3,* but does not express migratory NCC markers such as *Sox10* and *Vim* (Figure 2D). Subclusters 2' and 10' share a similar expression profile to subcluster 17'. However, subcluster 2' and 10' express less *Wnt1* and less neural plate border specifiers such as *Zic2* and *Pax7* than subcluster 17' (Figure 2D; Figure 2-figure supplement 1). This data suggests that subclusters 2' and 10' could represent EMT intermediate states as premigratory NCC transition to migratory NCC during delamination. Lastly, the remaining early NCC subclusters express *Sox10* and *Vim* indicating that they comprise or represent migratory NCC (Figure 2D).

To further validate the identity of subclusters 2' and 10' as representing intermediate cellular stages of EMT, we assessed the expression of genes associated with adherens junctions, tight junctions, and apical-basal polarity, which are required to maintain epithelial integrity, and cytoskeleton rearrangement that is typically associated with EMT (Dongre and Weinberg 2019; Matsuuchi and Naus 2013; Radisky and Radisky 2010) (Zhao and Trainor 2023). Intermediate NCC exhibit a decrease in *Nectin*, *Cadherin* and *Tight Junction Protein* gene expression consistent with intercellular tight junction breakdown and degradation of apicobasal polarity (Figure 2E). At the same time, subcluster 2 and 10 cells exhibit an increase in *Rac*, *Rack1* and *Cdc42* gene expression which is indicative of cytoskeletal rearrangement and the formation of

217 cell protrusions (Figure 2E). These alterations in gene expression are indicative of the molecular
218 cellular mechanisms that underpin EMT (Figure 2E).
219
220 **Mouse cranial NCC undergo EMT and delamination in S or G2/M phase cell cycle**
221
222 Since intermediate NCC stages represent a transitional or intermediate phase between
223 premigratory and migratory NCC, the molecular and signaling pathway signatures uniquely
224 expressed by these intermediate NCC can reveal essential regulatory mechanisms governing
225 NCC EMT and delamination. Analysis of cell cycle gene expression, for example, indicated that
226 EMT intermediate NCC populations exhibit distinct cell cycle phase properties or characteristics.
227 NCC in subcluster 2' primarily express S phase cell cycle genes such as *Pcna*, *Pol1* subunits, *Plk1*,
228 *Ccnd* and *Mcm* family members. In contrast, NCC in subcluster 10' predominantly express G2/M
229 phase cell cycle genes including *Mik67*, *Aurka/b*, *Cenp* and *Kif* family members (Figure 3A and
230 3B).
231 To understand the potential for any temporal or lineage relationships between the two
232 intermediate stage NCC populations based on their different cell cycle states, we performed
233 pseudotime trajectory analysis on the entire NCC population using Monocle 3 (Figure 3C and
234 3D). Premigratory and EMT intermediate NCC were identified as the earliest discrete
235 populations to form among the entire cranial NCC population (Figure 3C). In contrast, late
236 migratory NCC represent a more mature stage of NCC development (Figure 3C). Results from
237 the pseudotime analysis indirectly support the identities previously assigned to the cranial NCC
238 subclusters under both resolutions. The trajectory analysis also demonstrates that NCC can
239 arise through two independent paths and initially become two distinct intermediate
240 populations (subcluster 2' and 10') during EMT (Figure 3D). Later the trajectories or lineages of
241 the intermediate NCC subclusters then merge back together into a single or common
242 population of early migratory NCC, before ultimately maturing into still as yet undifferentiated
243 late migratory NCC as they colonize the frontonasal or pharyngeal arch mesenchyme (Figure
244 3D). These results imply that NCC representing two distinct intermediate stages form
245 simultaneously and independently during development. Moreover, the different cell cycle
246 status of subclusters 2' and 10' suggest that premigratory NCC can undergo EMT and
247 delamination in either S phase or G2/M phase of the cell cycle. The trajectory analysis further
248 depicts that EMT intermediate NCC and their immediate lineages are not fate restricted to any
249 specific cranial NCC derivative at this timepoint.
250
251 **Cell cycle regulation is critical for mouse cranial NCC EMT and delamination**
252
253 Since EMT intermediate NCC are either in S phase or G2/M phase of the cell cycle, we
254 then investigated whether cell cycle regulation plays a significant role in driving mouse cranial
255 NCC delamination. We dissected E8.5 *Wnt1-Cre;RosaeYFP* mouse embryos and examined the
256 expression of cell cycle markers to compare the cell cycle status of delaminating NCC at the
257 neural plate border in cranial tissues versus premigratory non-delaminating NCC in in the neural
258 plate border of the trunk. EdU and phospho-histone H3 (pHH3) were used to label S phase and
259 G2/M phase of the cell cycle respectively (Figure 4A). A majority of delaminating cranial NCC
260 express either EdU or pHH3 or both. Only a very small percentage of cells do not express either

261 of these cell cycle markers (Figure 4C). In contrast, almost 50% of premigratory, non-
262 delaminating trunk NCC in the dorsolateral neural tube, do not express either cell cycle marker
263 (Figure 4D). These observations imply that specific cell cycle phases are intimately connected to
264 mouse cranial NCC EMT and delamination.
265 To further validate the association between cell cycle status and cranial NCC EMT and
266 delamination, we inhibited S phase during early NCC development by incubating E8.0 CD1
267 mouse embryos in whole embryo roller culture with Aphidicolin. After 12 hours of treatment,
268 we quantified the number of migratory NCC via Sox10 immunostaining to determine the
269 number of premigratory NCC that delaminated. Cell cycle status was also evaluated in DMSO
270 (control) and Aphidicolin treated samples via EdU and pHH3 staining. Based on our trajectory
271 analyses, we hypothesized that inhibiting S phase progression would block S phase
272 delamination but not G2/M phase delamination. As we expected, the EdU signal was
273 completely absent in Aphidicolin treated embryos demonstrating that cells cannot enter S
274 phase post treatment (Figure 4-figure supplement 1). The Aphidicolin treatment did not induce
275 cell death as the level of TUNEL staining in treated embryos was similar to that observed in
276 controls (Figure 4-figure supplement 1). Quantification of Sox10 positive cells revealed
277 significantly fewer migratory neural crest cells in the craniofacial region of Aphidicolin treated
278 embryos compared to DMSO treated control embryos (Figure 4E). Similarly, we also treated
279 E8.0 *Mef2c-F10N-LacZ* embryos with Aphidicolin for 12 hours in roller culture and observed
280 fewer migratory NCC compared to control embryos as evidenced by LacZ staining (Figure 4-
281 figure supplement 1). Interestingly, pHH3 is expressed by a major proportion of the remaining
282 migratory NCC after Aphidicolin treatment (Figure 4B). This data is consistent with the
283 pseudotime trajectory analysis that cranial NCC delamination in G2/M phase of the cell cycle
284 (subcluster 10' NCC) is independent of delamination in S phase of the cell cycle (subcluster 2'
285 NCC). Disrupting S phase of the cell cycle didn't prohibit EMT intermediate NCC in G2/M phase
286 of the cell cycle from delaminating and forming migratory NCC that express G2/M phase cell
287 cycle markers. Thus, our data shows that cranial NCC delamination is disrupted upon S phase
288 cell cycle inhibition, which supports the hypothesis that cell cycle regulation is critical for cranial
289 NCC delamination in mouse embryos.
290
291 **Spatiotemporal localization of intermediate stage NCC *in vivo***
292
293 To identify and define EMT intermediate stage NCC *in vivo* during mouse cranial NCC
294 development, we used the scRNA-seq data to extract genes that were differentially expressed
295 (threshold based on average logFC ≥ 0.25) in the intermediate NCC populations (Figure 5-figure
296 supplement 1). Among the potential marker genes, we then selected *Dlc1*, *Sp5* and *Pak3* based
297 on their relatively high expression levels and specificity in cranial NCC, and more importantly,
298 intermediate NCC populations (Figure 5A; Figure 5-figure supplement 1). During cranial NCC
299 development, *Sp5* and *Pak3* are expressed at high levels in both premigratory and intermediate
300 stage NCC. In contrast, *Dlc1* is highly expressed in intermediate and migratory NCC (Figure 5A).
301 To further distinguish between premigratory, intermediate and migratory NCC, *Wnt1* (a
302 premigratory NCC marker) and *Sox10* (a migratory NCC marker) were also included in the *in situ*
303 identification analyses alongside *Dlc1*, *Sp5* and *Pak3* (Figure 5A).

To confirm that the intermediate stage markers *Dlc1, Sp5* and *Pak3* are expressed during NCC delamination, and determine the spatial location of the intermediate stage NCC, we performed signal amplification by exchange reaction for multiplexed fluorescent in situ hybridization (SABER-FISH). SABER-FISH was chosen for our multiplexed analyses of gene expression because SABER-FISH probes lack secondary structure which facilitates increased sensitivity and depth of tissue penetration. SABER-FISH oligo pools were designed for *Wnt1*, *Sox10, Dlc1, Sp5* and *Pak3,* using stringent parameters (Kishi et al. 2019). Intermediate stage marker probes were validated by comparing the expression patterns of the SABER-FISH staining for *Dlc1, Sp5* and *Pak3* with traditional in situ hybridization staining in transverse histological sections (Figure 5-figure supplement 2). The expression of *Dlc1, Sp5* and *Pak3* matched between SABER-FISH and traditional in situ hybridization methods, validating our probe design (Figure 5-figure supplement 2*).*

Following individual validation, we then performed combined staining to visualize the spatial distribution of all the genes in the same tissue section (Figure 5B). The intermediate stage markers *Dlc1, Sp5* and *Pak3* appeared to overlap in expression in the dorsal most region of the neural fold, where EMT takes place as evidenced by the presence of *Sox10* labelled migratory NCC adjacent to the neuroepithelium (Figure 5B). This overlap in expression was notably not observed in older embryos in areas where EMT had concluded. To better visualize and confirm co-localized expression of these genes in the same dorsolateral region of the neural plate border, we generated polyline kymographs depicting the average intensity of each gene's fluorescent signal along the dorsal most region of the neural fold and into the migratory NCC population (Figure 5C). We observed a consistent pattern of activity in which *Wnt1* is highly expressed in the dorsal neuroepithelium (Figure 5C). However, in the most dorsolateral domain, where *Wnt1* expression is slightly diminished, the intermediate stage NCC markers *Dlc1, Sp5* and *Pak3* are highly expressed (Figure 5C). In contrast, minimal *Sox10* expression is detected in this transition region at the edge of the neuroepithelium, but high levels of *Sox10* in the clear absence of *Wnt1, Dlc1, Sp5* and *Pak3,* is observed in migratory NCC located more ventrally (Figure 5C). Therefore, our data indicates that EMT intermediate stages can not only be transcriptionally defined, but also spatially resolved to the dorsal most region of the neuroepithelium.

EMT intermediate stage marker gene Dlc1 regulates NCC delamination

Having transcriptionally defined intermediate stage NCC and determined their special location during delamination, it was important to test whether any of the intermediate stage signature genes, *Dlc1*, *Pak3* or *Sp5*, play functional or essential roles in NCC development. We prioritized *Dlc1* over *Pak3* and *Sp5* because *Dlc1* is not expressed by premigratory NCC but is expressed at high levels in all EMT intermediate stage NCC. Furthermore, *Dlc1* null mutant mice are embryonically lethal and exhibit craniofacial malformation phenotypes, which is suggestive of a perturbation of NCC development. In contrast, *Pak3* and *Sp5* are expressed in premigratory NCC, but in only 50-60% of intermediate stage NCC (Figure 5A). Moreover, *Pak3* and *Sp5* null mutant mice are healthy and fertile with no obvious abnormalities. Therefore, we hypothesized that alone, *Dlc1* loss-of-function would more likely perturb cranial NCC delamination.

347 To test this hypothesis, we knocked down *Dlc1* by injecting *Dlc1* shRNA-based
348 lentiviruses and control scrambled shRNA lentiviruses into the amniotic cavity of E7.5 CD1
349 mouse embryos. Since the neural plate remains open at this developmental stage, all
350 neuroepithelial cells are exposed or in contact with amniotic fluid containing virus. The embryos
351 were then cultured for 24 hours after which we assessed the number of migratory NCC via
352 *Sox10* staining, to determine how many premigratory NCC underwent EMT and delamination
353 (Figure 6A). We subsequently observed that the number of migratory NCC was significantly
354 reduced in all *Dlc1* knockdown embryos (Figure 6B). In fact, each of the *Dlc1* shRNA constructs
355 led to a significant reduction in the number of migratory NCC compared to their respective
356 control (Figure 6-figure supplement 1*).* Importantly, we did not observe any difference in cell
357 death in *Dlc1* knockdown embryos comparable to controls (Figure 6D). On average, a 30%
358 reduction of *Dlc1* expression was achieved by each *Dlc1* shRNA lentivirus knockdown (Figure 6C;
359 Figure 6-figure supplement 1), and notably, the *Dlc1* isoforms targeted by the different *Dlc1*
360 shRNA constructs used in this study suggest a correlation with *Dlc1* null mouse embryos and
361 their phenotypes.
362 *Dlc1a* shRNA construct targets exon 1 specifically in *Dlc1* mRNA variant 2. Consequently,
363 *Dlc1a* shRNA is capable of exclusively eliminating the expression of *Dlc1* mRNA variant 2
364 (isoform 2) since the same exon region is not present in variant 1 or 3. Interestingly, one of the
365 *Dlc1* null mouse models, $Dlc1^{gt/gt}$, carries a gene trap vector inserted into intron 1, which results
366 in reduction of the 6.1 kb transcript (Dlc1 isoform 2) alone (Sabbir et al. 2010). Therefore, it is
367 possible that the craniofacial phenotypes observed in $Dlc1^{gt/gt}$ null mice are caused by abnormal
368 cranial NCC EMT and delamination as shown by *Dlc1a* knockdown in our data. In contrast, *Dlc1b*
369 and *Dlc1c* shRNA constructs both target exon 5 of *Dlc1* mRNA variant 2 and 3, which is the same
370 as exon 9 of variant 1. Consequently, all three *Dlc1* variants should be diminished by *Dlc1b* and
371 *Dlc1c* shRNAs. In another *Dlc1* null mouse model, exon 5 was deleted by replacing it with a
372 neomycin resistance gene, which caused a reading frame shift and subsequently premature
373 translation termination (Durkin et al. 2005). This led to the synthesis of truncated polypeptides
374 containing only the first 77 amino acids, which encode the sterile alpha motif (SAM) protein
375 interaction domain and 23 novel residues. Since $Dlc1^{-/-}$ null, *Dlc1b* and *Dlc1c* shRNAs all cause
376 disruptions in exon 5/9 of *Dlc1* transcripts, there is a strong correlation between the $Dlc1^{-/-}$ null
377 craniofacial phenotypes and cranial NCC EMT defects observed in *Dlc1b* and *Dlc1c* knockdown
378 mouse embryos. Collectively, these results therefore demonstrate an important functional role
379 for Dlc1 in mammalian NCC EMT and delamination. Moreover, our results suggest that genes
380 that are differentially expressed in intermediate NCC could play a regulatory role during EMT
381 and delamination.
382
383 **Discussion**

384 EMT is a cellular process that converts epithelial cells to mesenchymal cells. EMT is
385 essential for normal development and is a key driver of disease pathogenesis, particularly
386 cancer metastasis. Although classically considered to be a binary event, studies of EMT in
387 cancer identified multiple intermediate states within the EMT spectrum, a phenomenon termed
388 epithelial to mesenchymal plasticity (EMP). However, it remained to be determined whether
389 developmental EMT is also a developmental EMP process. Our goal therefore was to determine

390 whether intermediate stages of NCC development during EMT could be transcriptionally and
391 spatially defined, and then test whether transitional stage associated genes are functionally
392 required for NCC EMT and delamination.
393 Through scRNA-seq analysis of mouse cranial tissues at E8.5, which coincided with the
394 onset of NCC EMT and delamination, we identified two populations of NCC, whose gene
395 expression profiles or signatures were representative of intermediate stages between
396 premigratory and migratory NCC. Furthermore, we determined that the two intermediate
397 populations could be defined by their distinct transcriptional states which were consistent with
398 being in either S phase or G2/M phase of the cell cycle. Pseudotime trajectory analysis suggests
399 that these intermediate stage cranial NCC populations can undergo EMT and delaminate in
400 either S phase or G2/M phase, simultaneously, and independently of each other, but then later
401 merge into a single or common pool of early migratory NCC, suggesting they do not have
402 distinct fates following migration. This is consistent with the known plasticity and potency of
403 migrating NCC (Sandell and Trainor 2006; Trainor and Krumlauf 2000a; Trainor and Krumlauf
404 2000b, 2001).
405 These results correlate with observations that cell cycle status is also a critical factor
406 regulating NCC delamination in avian and zebrafish embryos. For example, BrdU incorporation,
407 which demarcates proliferating cells in S phase of the cell cycle, was previously used to evaluate
408 the cell cycle status of emigrating trunk NCC, dorsal midline neuroepithelial cells and
409 surrounding cells at the segmental plate, epithelial somite and dissociating somite axial levels in
410 chicken embryos (Burstyn-Cohen and Kalcheim 2002). Most emigrating trunk NCC (about 80%)
411 at the epithelial somite and dissociating somite axial levels were in S phase of the cell cycle,
412 while less than 50% of dorsal neuroepithelial cells were BrdU+. Similarly, slice culture of the
413 trunk of chicken embryos also revealed that most premigratory NCC contained basally
414 positioned nuclei indicative of S phase. Interestingly, however, a small proportion of
415 premigratory NCC presented as round mitotic cells, whose daughter cells later became
416 migratory (Ahlstrom and Erickson 2009). In comparison, *in vivo* time-lapse imaging of chicken
417 embryos revealed that half of the delaminating trunk NCC that were tracked, displayed signs of
418 cell division (McKinney et al. 2013). However, in most cases, only one progeny of a mitotic
419 premigratory NCC was observed to exit the neural tube and become a migratory NCC. In
420 contrast to delaminating trunk NCC, only around 30% of delaminating cranial NCC in chicken
421 embryos were found to be in S phase (Théveneau et al. 2007) illustrating considerable
422 differences between cranial and trunk neural crest cells and in the correlation between cell
423 cycle phase and delamination. Interestingly, time-lapse imaging of zebrafish embryos also
424 revealed active cell division in dorsal neuroepithelial cells prior to NCC delamination and EMT.
425 The daughter cells of those divisions then translocate into the basal side of the
426 neuroepithelium, where EMT subsequently occurs (Berndt et al. 2008). Whether delaminating
427 NCC undergo proliferation and cell division in zebrafish embryos remains to be investigated,
428 however, active cell division in the dorsal neuroepithelium is a shared feature of NCC
429 delamination in avian and aquatic species. Even though our findings primarily illustrate the
430 association of distinct cell cycle phases with intermediate stage NCC during EMT and
431 delamination, this work has emphasized the importance of further examining the cell division
432 and cell cycle activities of delaminating NCC in mouse embryos as critical contributors to normal
433 development and the pathogenesis of neurocristopathies.

434 Blocking G1/S transition in chicken embryos via *in ovo* electroporation, or via small
435 molecule inhibitors in explanted neural primordia, prevents the onset of NCC delamination
436 (Burstyn-Cohen and Kalcheim 2002). Furthermore, BMP and Wnt canonical signaling regulates
437 the G1/S transition and promotes trunk NCC delamination (Burstyn-Cohen et al. 2004).
438 Although it remains to be determined which signaling pathways regulate cell cycle phase
439 progression in the intermediate or transitional populations of NCC in mouse embryos, our
440 results illustrate an evolutionarily conserved mechanistic role for cell cycle progression in NCC
441 delamination in vertebrate embryos.
442 The intermediate populations of cranial NCC in mouse embryos exhibited
443 transcriptional profiles that were characterized by the downregulation of tight junction and
444 polarity genes. This is consistent with the breakdown of intercellular tight junctions and
445 degradation of apicobasal polarity, which are hallmarks of EMT (Zhao and Trainor 2023).
446 Further interrogation of genes that were differentially expressed in the intermediate NCC
447 populations revealed *Dlc1*, *Sp5* and *Pak3* based on their relatively high expression levels as
448 potentially specific markers, and regulators of intermediate NCC populations. Through SABER-
449 FISH staining of *Dlc1*, *Sp5* and *Pak3* in combination with *Wnt1* as a marker of premigratory NCC,
450 and *Sox10* as a marker of migratory NCC, we spatially resolved the location of intermediate NCC
451 to the most dorsolateral domain of the cranial neural plate in E8.5 mouse embryos. We then
452 prioritized *Dlc1* for functional analyses because it is expressed at high levels in all EMT
453 intermediate stage NCC, but not in premigratory NCC. Lentiviral shRNA knockdown of *Dlc1* in
454 cultured mouse embryos resulted in a significant reduction in the number of migratory neural
455 crest cells, which may account for the craniofacial and cardiac malformation phenotypes
456 observed in *Dlc1* null mutant mice (Sabbir et al. 2010). Thus *Dlc1*, which is primarily expressed
457 in intermediate stage NCC, plays an important role in NCC EMT and delamination. Dlc1 is a Rho
458 GTPase Activating Protein (GAP) that regulates the activity of Rho family GTPases Rho and
459 Cdc42 (Kim et al. 2008). RhoGTPases are known to regulate cell morphology and motility
460 through modulating the activity of the actin cytoskeleton. More specifically, Rho has been
461 shown to facilitate the formation of stress fibers, while Cdc42 is involved in filopodium
462 formation (Kim et al. 2008). RhoGTPases also regulate the organization of tight junctions, which
463 breakdown during EMT (Popoff and Geny 2009; Terry et al. 2010). Therefore, the effect of *Dlc1*
464 knockdown on cranial NCC EMT and delamination may be mediated via disrupted RhoGTPase
465 activity and subsequent downstream cellular changes.
466 A similar regulatory role for Dlc1 and other GAP family members has also been observed
467 during NCC EMT and delamination in chicken and zebrafish embryos. In chicken embryos, *Dlc1*
468 overexpression results in ectopic trunk NCC delamination, including apically into the neural
469 tube lumen, due to a disruption in apical-basal polarity of dorsal neuroepithelial cells (Liu et al.
470 2017). Furthermore, NCC overexpressing *Dlc1* exhibit a loss of directionality during migration.
471 Conversely, *Dlc1* inhibition and depletion results in less NCC emigration and thus fewer
472 migratory NCC. In addition, the downregulation of *Dlc1* in migrating NCC restricts their motility.
473 Thus, *Dlc1* regulates trunk NCC delamination and migration in chicken embryos. Interestingly, in
474 zebrafish embryos, another GAP family member Arhgap has been shown to modulate NCC EMT
475 and delamination via the localization of Rho activation to designated subcellular compartments
476 and the promotion of localized actomyosin contraction to trigger directional cell motility (Clay
477 and Halloran 2013). More specifically, the knockdown of Arhgap in NCC results in Rho

activation, which in turn inhibits NCC EMT and delamination. These data suggest that the role of Dlc1 during NCC delamination might be evolutionarily conserved in vertebrate embryos. However, whether Dlc1 regulates mouse cranial NCC delamination through localized activation of Rho remains to be determined. Nevertheless, consistent with similarities in EMT, delamination and cell migration between neural crest cells and cancer cells, Dlc1 may also play an important role in promoting cell migration during cancer progression. High levels of DLC1 expression are detected in most melanoma tissues, and functional studies have revealed that DLC1 is both sufficient and required for melanoma growth and metastasis (Yang et al. 2020b).

In conclusion, through scRNA-sequencing we transcriptionally identified two distinct intermediate stages of NCC during EMT and delamination based primarily on cell cycle status. Delamination in S phase or G2/M phase seems to occur simultaneously but also independently, resulting in a single or common pool of early migratory NCC. Further interrogation of our transcriptomic dataset revealed *Dlc1* to be a key molecular marker of intermediate stage NCC, and their location in situ in the dorsolateral neural plate, which we spatially resolved in E8.5 mouse embryos. Lastly, we tested and functionally validated that *Dlc1* plays an important role in NCC delamination in mouse embryos. Taken together, our identification and characterization of intermediate stage cranial NCC during their delamination are consistent with NCC EMT being a developmental EMP event. Similar to intermediate EMT states in cancer metastasis, NCC downregulate certain epithelial cell features but maintain co-expression of epithelial cell markers and mesenchymal cell markers during EMT and delamination. Additionally, intermediate stage NCC are localized at the dorsolateral edge of the neural plate border, which is reminiscent of the localization of intermediate EMT states at the leading edge of invasion in several types of primary tumors. However, unlike certain intermediate EMT cells present in the lymph nodes or circulating tumor cells, mouse EMT intermediate NCC represent a transient state and eventually form migratory NCC with mesenchymal character. This suggests that EMP may be a more common developmental phenomenon. Our transcriptional data and signatures of intermediate stage NCC during EMT and delamination can serve as a useful resource for the community. This also now sets the stage for uncovering the gene regulatory networks that govern intermediate stage NCC development and function, and for exploring whether EMP is a feature of other developmental and pathological EMT events such as in gastrulation, wound healing, and fibrosis.

Materials and Methods

Mice and animal husbandry

All mice were kept in a 16h-light and 8h-dark light cycle in the Laboratory Animal Services Facility at the Stowers Institute for Medical Research. All animal experiments were conducted in accordance with Stowers Institute for Medical Research Institutional Animal Care and Use Committee (IACUC)-approved protocol (IACUC no. 2022-143). *Wnt1-Cre* mice (*H2afv*$^{Tg(Wnt1\text{-}cre)11Rth}$ Tg(Wnt1-GAL4)11Rth/J, Jax stock #003829) and *RosaeYFP* mice were obtained from the Jackson Laboratory and maintained and genotyped as previously described (Chai et al. 2000; Jiang et al. 2000). *Wnt1-Cre* was maintained as a heterozygous allele and crossed to homozygous *RosaeYFP* to generate *Wnt1-Cre;RosaeYFP*. *Mef2c-F10N-LacZ* mice, in

which LacZ expression is regulated by a neural crest cell specific enhancer of *Mef2c*, were maintained and genotyped as previously described (Aoto et al. 2015).

Immunohistochemistry

Wholemount

Embryos were dissected and fixed in 4% PFA (in PBS) overnight. The next day the embryos were rinsed 3 times for 5 minutes in PBS, dehydrated through an increasing methanol series from 25% methanol/PBS to 100% methanol and stored at -20°C until needed. Embryos were incubated in Dent's bleach (4:1:1 Methanol:DMSO:Hydrogen peroxide) for 2 hours in the dark at room temperature, rinsed in 100% methanol for 15 minutes, and rehydrated through a decreasing methanol series from 100% methanol to PBT (0.1% Triton in 1X PBS). Embryos were blocked in 2% goat serum + 2% Bovine Serum Albumin for 2 hours at room temperature before primary antibody (GFP, 1:500, Invitrogen #A6455) was added and the embryos were incubated overnight at 4°C with rocking. Embryos were washed three times for 5 minutes in PBT and then 6 times for 1 hour at room temperature with rocking. Embryos were incubated in secondary antibody (Alexa Fluor 488 Goat anti-Rabbit, 1:500, Invitrogen #11008; DAPI, 1:1200, Sigma-Aldrich #D9564) at 4°C in the dark overnight with rocking, then washed 3 times for 5 minutes in PBT and 6 times for 1 hour at room temperature with rocking. Embryos were then mounted in VECTASHIELD® Antifade Mounting Medium with DAPI (Vector Laboratories #H-1200) for imaging.

Cryosection

Embryos were dissected and fixed in 4% PFA (in PBS) overnight. Embryos were then transferred to 1X PBS and rocked for 10 minutes at 4°C, before being incubated in 30% sucrose in 1X PBS, at 4°C for 30 minutes-5 hours with rocking (or until embryos were equilibrated as indicated by their sinking to the bottom of the tube). Embryos were embedded in Tissue-Tek O.C.T. Compound (VWR #25608-930), sectioned transversely at 10um thickness on a NX70 Cryostar cryostat, permeabilized 3 times for 5 minutes in PBT, and blocked in 2% goat serum + 2% Bovine Serum Albumin for 2 hours at room temperature. Sections were then incubated in primary antibody overnight at 4°C and the following primary antibodies were used: Sox10 (1:500, Abcam #ab155279), phospho-histone H3 (1:500, Millipore #05-806), GFP (1:500, Invitrogen #G10362). Sections were then washed 3 times for 5 minutes in PBT at room temperature, before diluted secondary antibody and/or conjugated primary antibody solutions were added and the sections were incubated for 2 hours in the dark at room temperature. Sections were washed 3 times for 5 minutes in PBT before mounting in VECTASHIELD®. Secondary antibodies included Alexa Fluor 488 Goat anti-Rabbit (1:500, Invitrogen, #11008), 546 Goat anti-Mouse (1:500, Invitrogen, #A21045), 647 Goat anti-Rat (1:500, Invitrogen, #A21267), 647 Donkey anti-Mouse (1:500, Invitrogen, #A32787), DAPI (1:1200, Sigma-Aldrich, #D9564).

TUNEL staining

561 Cryosections were washed 3 times for 5 minutes in PBT and then permeabilized in 0.1%
562 sodium citrate/PBT for 5 minutes. Cryosections were then washed 3 times for 5 minutes in PBT
563 before being incubated with 1:10 TUNEL enzyme buffer (Roche #12156792910) at 37°C in the
564 dark for 2 hours. Sections were washed 3 times for 5 minutes in PBS prior to counterstaining
565 with DAPI and/or mounting in VECTASHIELD®.
566
567 **EdU labeling**

568 EdU staining was performed on cultured whole mouse embryos. Briefly, complete media
569 containing 50% DMEM-F12-Glutamax, 50% rat serum, and 1X penicillin/streptomycin was pre-
570 warmed at 37°C in roller culture bottles in a 5% CO2, 5% O2 and 90% N2 atmosphere (Muñoz
571 and Trainor 2019; Sakai and Trainor 2014). After E8.5 CD1 embryos were dissected in Tyrode's
572 buffer with an intact yolk sac, and equilibrated in culture media for 30 minutes, EdU (Invitrogen
573 #C10638) was added to the media according to the manufacturer's protocol at a working
574 concentration of 500uM. DMSO was added to control embryos. Embryos were then incubated
575 for 15 minutes, after which they were briefly rinsed in warm equilibrated culture media
576 followed by Tyrode's buffer before fixing in 4% PFA (in PBS) overnight at 4°C. Fixed embryos
577 were embedded and sectioned at 10um, and then stained following the manufacturer's
578 instructions, with fluorescent immunostaining performed as needed after EdU staining.
579

580 **Single cell RNA sequencing**

581 Tissue collection, cell processing and sequencing, and data processing were performed
582 as previously described (Falcon et al. 2022). Briefly, 6 *Mef2c-F10N-LacZ* (Aoto et al. 2015) and 6
583 *Wnt1-Cre;*RosaeYFP (Chai et al. 2000) E8.5 mouse embryos were collected, dissociated into
584 single cells, and 12,000-15,000 cells per sample were loaded on a Chromium Single Cell
585 Controller (10x Genomics). Libraries were prepared using the Chromium Next GEM Single Cell 3'
586 Library & Gel Bead Kit v3.1 (10x Genomics), quality control checked, and then pooled at equal
587 molar concentrations and sequenced on an Illumina NovaSeq 6000 S1 flow cell. Raw
588 sequencing data was processed using Cell Ranger (v3.0.0, 10x Genomics) and after
589 mitochondria and other feature thresholding, the final dataset used for analysis consisted of
590 21,190 cells (12,498 cells for Wnt1-Cre;RosaeYFP and 8,692 for Mef2c-F10N-LacZ and 29,041
591 genes, and is available at the Gene Expression Omnibus (accession no. GSE168351). R (v3.6.1)
592 was used for downstream analysis. The Seurat package (v3.1.5.9003) (Stuart et al. 2019) was
593 used to normalize data via the SCTransform method (Hafemeister and Satija 2019). For
594 clustering, 3000 highly variable genes were selected, and the first 46 principal components
595 based on those genes were used to identify 6 initial clusters at a resolution of 0.05 using the
596 shared nearest neighbor method. Cranial NCC were identified as one of the 6 initial clusters
597 based on the expression of tissue specific marker genes. The cranial NCC cluster was then
598 subdivided at resolution=0.26 into 5 subclusters, three of which were characterized as the early
599 migratory NCC based on NCC development gene expression. Early migratory NCC were further
600 subdivided into 15 subclusters at resolution=2.0 to explore the presence of EMT intermediate
601 NCC.
602

603 **Pseudotime trajectory analysis**

604 Trajectory analysis was performed using Monocle3 (0.2.2) with closed loop set to true
605 and use partition set to false on cranial neural crest cells, which were subset from the single cell
606 data set after doublet identification with DoubletFinder (2.0.2). The resulting pseudotime
607 estimates were added back to the Seurat metadata table for visualization and the trajectory
608 was plotted on the original clusters identified in the Seurat analysis.
609

610 **SABER-FISH staining and imaging**

611 All oligo pools, concatemer hairpins and fluorophore probes were designed and ordered
612 through IDT using stringent settings as previously described (Kishi et al. 2019). Only
613 fluorophores 488, 594 and 647 were used to prevent overlap in spectral emission and channel
614 bleed-through. SABER-FISH probes for each gene were made following the PER
615 concatamerization protocol. The probes were allowed to elongate for 2 hours at 37°C before
616 heat inactivation of the polymerase. A sample of the probes was run on a gel to confirm
617 elongation length and ensure that no secondary products had formed in the process. Probes
618 were then cleaned using the Qiagen PCR Purification kit and the final concentration of the
619 generated probes were measured by Nanodrop.
620 CD1 embryos were collected at the 5-6ss and fixed overnight in 4% PFA (in PBS) at 4°C.
621 Embryos were then washed 5 times in PBS with DEPC-PBTW (1X DEPC-PBS + 0.1% Tween-20)
622 and transferred into 30% sucrose PBTW and rocked overnight at 4°C. Next, embryos were
623 embedded in OCT, frozen and cryosectioned at 20µm thickness. Sections were placed on
624 Histogrip treated slides and warmed to encourage adherence, washed 3 times for 5 minutes in
625 PBTW, incubated in Hybridization wash buffer and allowed to equilibrate to 37°C (the lowest
626 melting temperature limit out of our probe set). Sections were then incubated with pre-
627 equilibrated probes overnight (roughly 16 hours) at 37°C. The next day the sections were
628 washed with Hybridization wash buffer, 2X SSCT (2×SSC + 0.1% Tween-20) and PBTW and then
629 the first set of fluorophores were applied to the sections [set one: Sox10, Wnt1 and Sp5; set
630 two: Pak3 and Dlc1] and left to hybridize at 37°C for 30 minutes. Following fluorophore probe
631 hybridization, sections were washed in PBTW with 1:1000 DAPI for 10 minutes followed by
632 PBTW 2 times for 5 minutes. The slides were then mounted in VECTASHIELD® containing DAPI
633 with a 1.5 glass coverslip.
634 Sections were imaged with a Nikon CSU-W1 inverted spinning disk equipped with a
635 sCMOS camera. Each laser was set to 400µs acquisition speed and a z-stack of 32 slices (1µm
636 per slice) was acquired. Following imaging of the first set of probes, the coverglass was gently
637 removed from each slide. The first set of fluorophore probes were removed by washing 3 times
638 for 5 minutes in PBTW washes, followed by 3 washes with Displacement buffer and another 3
639 washes in PBTW. Slides were remounted with VECTASHIELD®, covered with a coverslip and
640 imaged to ensure all previous fluorescent probes had been removed. After imaging, the
641 coverslip was removed again, and the sections were rinsed in PBTW. 3 times for 5 minutes. The
642 second fluorophore probes were then applied to the sections and allowed to hybridize for 30
643 minutes at 37 °C. Slides were then washed 3 times for 5minutes in PBTW and mounted a final

644 time in VECTASHIELD® containing DAPI. The second set of probes were imaged using the exact
645 same parameters as the first.
646
647 **SABER-FISH image processing**

648 All image processing was performed in FIJI/ImageJ (Schindelin et al. 2012) and plugin
649 source code can be accessed through https://github.com/jayunruh/Jay_Plugins. Plugins can be
650 used by following the Stowers Fiji update site. Convenience macros that combine these plugin
651 functionalities are included in the supplemental materials.
652 After acquisition, images were scaled by 0.5 with averaging (i.e. binning). Background
653 subtraction was run on the scaled images using the "roi average subtract jru v1" plugin. This
654 plugin takes the average intensity signal in a selected region of interest or chosen area of
655 background in the image and removes that average across the image. The two series of z-stack
656 images acquired for each set of probes were then aligned and combined through a
657 "registration_macro.ijm". In summary, this macro registers the two z-stacks according to DAPI
658 signal from a selected representative z-slice. Alignment is achieved through using an
659 implementation of the TurboReg tool set to a rigid body transformation (Thevenaz et al. 1998).
660 Once the two sets of probes have been aligned, the signals are measured and tracked
661 with the macro "all_combined_aftersubreg.ijm". Images were first copied, and then sum
662 projected in z before undergoing a Gaussian blur with sigma value 4. Nuclei are then identified
663 in the DAPI channel by a maximum finding approach with a minimum spot distance of 70 pixels
664 and a threshold of 10% of the maximum intensity (Varberg et al. 2022). Those spots provided a
665 locational value for later mapping of transcript signals in two dimensions. Individual transcripts
666 are found in three dimensions in the original combined images with a Gaussian blur with sigma
667 value 1 and a rolling ball background subtraction with a radius of 10 pixels. Because the signal is
668 very punctate and slides can accumulate auto-fluorescent debris over the course of staining, we
669 next removed the 20 brightest spots in 3D with a spheroid of xy diameter 15 and z diameter 5
670 to ensure we were evaluating true signal. Spots were found using the same maximum finding
671 approach as above but in 3 dimensions with a minimum separation of 12 pixels in xy and 4
672 slices in z and a threshold at 7% of the maximum intensity in each channel. The positions of
673 those found maxima were then sum projected in z to estimate the number of transcripts in the
674 vicinity of each nuclear maximum (see above).
675 An image showing the number of transcripts per cell was generated using
676 "make_nuclear_image.py" macro based on the nuclei and transcript locations identified in the
677 previous step. To generate the polyline kymograph showcasing spatial expression through the
678 tissue, a zoomed in region of the transcript mapped images was generated around the dorsal
679 neural fold tips. A line of 100 pixel width was drawn starting from the middle of the
680 neuroepithelium towards the dorsal most tip of the neural fold and then ventrally into the
681 underlying mesoderm and migratory neural crest cell population. The polyline kymograph was
682 generate based on this line using the plugin "polyline kymograph jru v1".
683
684 **RNA in situ hybridization**

685 *Dlc1, Pak3* and *Sp5 in situ* plasmids were previously published (Dunty et al. 2014;
686 Piccand et al. 2014). RNA in situ hybridization was performed as follows: Embryos were
687 rehydrated through a descending methanol series from 100% methanol to DEPC-PBTW, then
688 washed 2 times for 5 minutes in DEPC-PBTW. Embryos were bleached in 6% hydrogen peroxide
689 in the dark for 15 minutes with rocking and then incubated in 10µg/ml Proteinase K in DEPC-
690 PBTW for 4-5 minutes at room temperature, without rocking. Embryos were wash with 2 mg/ml
691 glycine in DEPC-PBTW for 5 minutes, then 2 times for 5 minutes in DEPC-PBTW before being
692 refixed in 4% DEPC-PFA + 0.2% glutaraldehyde for 20 minutes. Embryos were then washed 3
693 times for 5 minutes in DEPC-PBTW, rinsed in prewarmed (68°C) hybridization buffer (50%
694 formamide, 5X SSC pH 4.5, 0.05% EDTA pH 8, 0.2% Tween20, 0.1% CHAPS, 20mg/ml Boehringer
695 blocking powder, 1 mg/ml torula RNA, 0.05 mg/ml heparin), and incubated in hybridization
696 buffer with rocking for 1 hour at 68°C. Embryos were then incubated in digoxygenin-labeled
697 riboprobes (~2 ng/ul) in hybridization buffer overnight at 68°C. Day 2: Embryos were washed 2
698 times for 30 minutes with hybridization buffer at 68°C. followed by prewarmed Solution I (50%
699 formamide, 1X SSC pH 4.5, 0.1% Tween20), 3 times for 30 minutes at 65°C. Embryos were then
700 washed in 50% Solution I/50% MABT (1X MAB – Maleic acid, 0.1% Tween-20) for 30 minutes at
701 room temperature, followed by MABT, 3 times for 5 minutes. Embryos were then blocked in
702 MABT + 2% Boehringer blocking powder for 1 hour at room temperature, followed by MABT +
703 2% Boehringer blocking powder + 20% heat-treated goat serum for 2 hours. Embryos were then
704 incubated overnight in anti-digoxygenin-AP diluted 1:2000 in MABT + 2% Boehringer blocking
705 powder + 20% heat-treated goat serum, at 4°C. The embryos were then rinsed in MABT,
706 washed 2 times for 15 minutes in MABT, followed by 5-8 further washes in MABT for 1-1.5
707 hours each, and an overnight wash in MABT at room temperature. The embryos were then
708 washed 3 times for 10 minutes in NTMT (100mM NaCl, 100mM Tris pH 9.5, 50mM MgCl2, 0.1%
709 Tween-20), and incubated in NTMT + BCIP/NBT at room temperature in the dark. Color
710 development at room temperature was allowed to continue until the desired darkness of the
711 substrate was achieved. The color reaction was stopped by washing in PBTW, after which the
712 embryos were stored. long-term in 4% PFA (in PBS)/0.1% glutaraldehyde at 4 ºC. Stained
713 embryos were imaged, and sectioned transversely at 10um thickness prior to imaging.
714
715 **Aphidicolin treatment**

716 E7.5-E8.0 CD1 embryos were dissected in Tyrode's buffer with their yolk sac intact and
717 incubated in pre-warmed culture media for 30 minutes-1 hour as previously described (Muñoz
718 and Trainor 2019; Sakai and Trainor 2014, 2016). After 30 minutes equilibration, 0.5ug/ml
719 aphidicolin (Sigma-Aldrich, #A0781) was added to the culture media to inhibit S phase of the
720 cell cycle. The same quantity of DMSO was added to the control embryos. Following 12-13
721 hours of roller culture, EdU as added during the final 15 minutes. Embryos were then fixed in
722 4% PFA (in PBS) overnight at 4°C. overnight. Fixed embryos were embedded and sectioned at
723 10um and stained using the EdU kit following the manufacturer's instructions. Sox10 and
724 phospho-histone H3 fluorescent immunostaining was performed after EdU staining as
725 described above. TUNEL staining (described above) was performed after fluorescent
726 immunostaining if applicable.
727

728 **ShRNA-based lentiviral plasmids and lentivirus production**

729 A shRNA plasmid clone set targeting *Dlc1* was obtained from GeneCopoeia
730 (MSH100727-LVRU6MP). Each set contains 3 shRNA expression constructs and 1 scrambled
731 shRNA control. Each shRNA hairpin consists of a 7 base loop and 19-29 base stem optimized for
732 specific gene sequences as detailed by the manufacturer. Glycerol stocks of shRNA-based
733 lentiviral plasmids were cultured in LB buffer with 100 µg/ml of ampicillin (Amresco # 0339).
734 Plasmids were purified using a HiSpeed Plasmid midi kit (Qiagen #12643).
735 A total of $4e^6$-$5e^6$ of 293T cells were seeded in one 10cm plate with 12ml of media
736 without antibiotics the day before transfection. On the following day, when the cells reached
737 70-80% confluence, transfection was performed as follows: shRNA-based lentiviral plasmids
738 (7ug), Pax2 packaging plasmid (7ug) and VSVG envelop plasmid (1ug) were mixed with 45ul of
739 Fugene HD transfection reagent (Promega, cat#E5911) in 1.5ml of Opti-MEM (Gibco,
740 cat#31985070). The mixture was incubated at room temperature for 15 minutes and then
741 added dropwise to the plate of 293T cells. Virus-containing old culture media was harvested
742 after 48 hours and 72 hours upon transfection. We then mixed the virus-containing media and
743 added HEPES to reach 10mM final concentration. The media was spun down at 500g for 5
744 minutes at 4°C to remove cell debris and the supernatant was then collected and filtered
745 through 0.45um filter into a falcon tube. We added 1 volume of 4x lentivirus concentrator
746 solution (40% PEG-8000 in 1.2M NaCl) to 3 volumes of the filtered virus, mixed well and placed
747 the tube on a shaker (60rpm/minute) at 4°C for overnight. The filtered virus was centrifuged at
748 1600g for 1hour at 4°C and the supernatant was carefully removed without disturbing the
749 pellet. The pellet was then thoroughly resuspended with 1ml of cold PBS by gently pipetting up
750 and down. The solution was transferred to 1.5ml tube and placed at room temperature for 10
751 minutes. We gently pipetted the virus again about 20 times and spun it down in a
752 microcentrifuge at full speed for 3 minutes to pellet the protein debris. The supernatant was
753 then aliquoted and stored at -80°C for future use.
754
755 **Lentivirus injection**

756 E7.5-E8.0 CD1 embryos were dissected in Tyrode's buffer with an intact yolk sac and
757 equilibrated in pre-warmed culture media for 30 minutes as previously described (Muñoz and
758 Trainor 2019; Sakai and Trainor 2014, 2016). Viruses in 5ul aliquots were thawed and kept on
759 ice, then pipetted onto a piece of parafilm in a small dish with the lid on to prevent
760 evaporation. Using the Eppendorf CellTram Vario system, 1-2ul of each virus was injected into
761 the amnionic cavity of each embryo (or until the amnion had visibly expanded) after which
762 time, the embryos were returned to roller culture. After 24 hours of incubation, embryos were
763 rinsed in PBS and fixed in 4% PFA (in PBS) at 4°C overnight. Fixed embryos were imaged,
764 embedded, and sectioned at 10um thickness before fluorescent immunostaining with Sox10.
765
766 **RNA isolation, cDNA preparation and quantitative reverse transcription-PCR (qRT-PCR)**

767 Individual E8.5 mouse embryo head and tail tissues post culturing were collected into
768 1.5mL tubes and flash froze on dry ice with minimal DEPC-Tyrode's buffer remained in the tube.
769 RNA was extracted using the Qiagen miRNeasy Micro Kit (Qiagen #217084) with on-column

770 DNase treatment. RNA concentration was determined by Nanodrop. The SuperScript™ III First-
771 Strand Synthesis System (Invitrogen #18080051) was used to synthesize cDNA for qRT-PCR with
772 random hexamer primers, and qRT-PCR was performed on an ABI7000 (Thermo QuantStudio 7)
773 using Perfecta SYBR Green (Quantbio #95072-250). Primers are listed in Supplemental Table 2.
774 No template and no reverse transcription controls were run as negative controls. ΔΔCt method
775 was used to calculate fold change. One-way ANOVA was used for statistical analysis and
776 significance was determined based on $p < 0.05$.
777
778 **β-galactosidase staining**

779 E8.5 *Mef2c-F10N-LacZ* embryos were collected and fixed in 2% formalin, 0.2%
780 glutaraldehyde in 1X PBS for 15-20 minutes. Embryos were rinsed with PBS and stained
781 according to manufacturer's protocol (Millipore #BG-6-B, #BG-7-B, #BG-8-C). Embryos were
782 then fixed again in 4% PFA (in PBS) at 4°C with rocking overnight followed by washing in PBS for
783 whole embryo brightfield imaging.
784
785 **Fluorescent imaging**

786 Fluorescently stained section images were captured on an upright Zeiss LSM-700 laser
787 scanning confocal microscope using 405 nm, 488 nm, 555 nm and 639 nm excitation lasers.
788 Emissions filters used to acquire images were Far-red: LP 640nm, Red: BP 505-600 nm, GFP: BP
789 490-555 nm, DAPI: SP 490 nm. Images were acquired with a Zeiss Fluar 10x objective lens. For
790 each specimen, a z-stack of images was collected and processed as a maximum intensity
791 projection.
792 All the images used for quantification were acquired with an Orca Flash 4.0 sCMOS
793 100fps at full resolution on a Nikon Eclipse Ti2 microscope equipped with a Yokagawa CSU W1
794 10,000 rpm Spinning Disk Confocal system. The spinning disk confocal is equipped with a quad
795 filter for excitation with 405/488/561/640. Emissions filters used to acquire images were Far-
796 red: 669-741nm, Red: 579-631 nm, GFP: 507-543 nm, DAPI: 430-480 nm. A Nikon Plan
797 Apochromat Lambda LWD 40x objective was used to acquire the images with 50-100 ms
798 exposure times.
799
800 **Image processing**

801 All analyses of fluorescent intensity were performed using Fiji and custom-written
802 ImageJ Macro and python notebooks. Prior to the analyses, raw images were processed by
803 subtracting background and were then projected for the max intensity to form single multiple-
804 color images. Individual cells were segmented based on DAPI channel with a pre-trained
805 cellpose model (Stringer et al. 2021), and then the mean intensity of the individual channel was
806 measured by FIJI. The segmented cells were classified as either positive or negative based on
807 their intensity in the corresponding channel. For images from the shRNA lentivirus injection
808 experiments, due to the large variety of background signals, we manually labeled positive cells
809 and then trained a cellpose model based on the manually labeled cells. Positive cells were
810 classified based on the trained model, and their coordinates were recorded and saved to
811 ImageJ ROI files for future verification.

For the cell cycle staining analysis, cells in the most dorsal lateral domain of the cranial and trunk neural plate were selected and saved to ImageJ ROI files. In cranial neural plate border cells, the following quantifications were performed: EdU+%=the percentage of EdU positive cells within eYFP positive delaminating premigratory NCC; pHH3+%= the percentage of pHH3 positive cells within eYFP positive delaminating premigratory NCC; EdU+pHH3+%= the percentage of EdU and pHH3 double positive cells within eYFP positive delaminating premigratory NCC; EdU-pHH3-%= the percentage of EdU and pHH3 double negative cells within eYFP positive delaminating premigratory NCC. In trunk neural plate border cells, the following quantifications were performed: EdU+%=the percentage of EdU positive cells within DAPI positive neural plate border cells at the trunk axial level; pHH3+%= the percentage of pHH3 positive cells within DAPI positive trunk neural plate border cells; EdU+pHH3+%= the percentage of EdU and pHH3 double positive cells within DAPI positive trunk neural plate border cells; EdU-pHH3-%= the percentage of EdU and pHH3 double negative cells within DAPI positive trunk neural plate border cells. For the Aphidicolin treatment experiments, neuroepithelial cells and Sox10 positive migratory NCC were selected and saved to ImageJ ROI files. The ratio of Sox10 positive migratory NCC over DAPI positive neural plate/neuroepithelial cells was calculated. For the shRNA lentivirus injection experiments, Sox10 positive migratory NCC were selected and saved to ImageJ ROI files. The number of Sox10 positive cells was quantified.

Brightfield imaging

Embryos were imaged on a Leica MZ16 microscope equipped with a Nikon DS-Ri1 camera and NIS Elements imaging software. Manual Z stacks were taken and then assembled using Helicon Focus software. Sections from embryos stained by in situ hybridization were imaged on a ZEISS Axio Vert and stitched using ImageJ if needed.

Acknowledgements

We thank members of the Trainor laboratory for their insights and suggestions on the project. We also acknowledge our amazing animal technician, Melissa Childers, and the Laboratory Animal Services facility at Stowers Institute for Medical Research for animal husbandry and care of the mice used in this work. The *Dlc1*, *Sp5* and *Pak3* ISH plasmids were generously provided by Dr. Marian Durkin, Dr. Gerard Gradwohl, and Dr. Terry Yamaguchi, respectively. We also thank Mark Miller, who created the beautiful illustration for the experimental workflow included in Figure 1. Funding for this research was provided by the Stowers Institute for Medical Research (P.A.T) and the National Institute for Dental and Craniofacial Research F31 DE032256 (E.L.M.). The scRNA-seq data was generated through the University of Kansas Medical Center Genomics Core. Funding for the Genomics Core services was provided by the Kansas Intellectual and Developmental Disabilities Research Center (NIH U54 HD 090216), the Molecular Regulation of Cell Development and Differentiation – COBRE (P30 GM122731-03)

852 and the NIH S10 High-End Instrumentation Grant (NIH S10OD021743) at the University of
853 Kansas Medical Center, Kansas City, KS 66160.

854 **References**

855 Achilleos A, Trainor PA. 2015. Mouse models of rare craniofacial disorders. Review of. *Curr Top Dev Biol*
856 **115**:413-458. doi: 10.1016/bs.ctdb.2015.07.011
857 Ahlstrom JD, Erickson CA. 2009. The neural crest epithelial-mesenchymal transition in 4d: A 'tail' of
858 multiple non-obligatory cellular mechanisms. Review of. *Development (Cambridge, England)*
859 **136**:1801-1812. doi: 10.1242/dev.034785
860 Aoto K, Sandell LL, Butler Tjaden NE, Yuen KC, Watt KEN, Black BL, Durnin M, Trainor PA. 2015. Mef2c-
861 f10n enhancer driven β-galactosidase (lacz) and cre recombinase mice facilitate analyses of gene
862 function and lineage fate in neural crest cells. Review of. *Developmental Biology* **402**:3-16. doi:
863 10.1016/j.ydbio.2015.02.022
864 Aybar MJ, Nieto MA, Mayor R. 2003. Snail precedes slug in the genetic cascade required for the
865 specification and migration of the xenopus neural crest. Review of. *Development (Cambridge,*
866 *England)* **130**:483-494. doi: 10.1242/dev.00238
867 Berndt JD, Clay MR, Langenberg T, Halloran MC. 2008. Rho-kinase and myosin ii affect dynamic neural
868 crest cell behaviors during epithelial to mesenchymal transition in vivo. Review of.
869 *Developmental Biology* **324**:236-244. doi: 10.1016/j.ydbio.2008.09.013
870 Bhatt S, Diaz R, Trainor PA. 2013. Signals and switches in mammalian neural crest cell differentiation.
871 Review of. *Cold Spring Harbor Perspectives in Biology* **5**:a008326. doi:
872 10.1101/cshperspect.a008326
873 Bulfone A, Kim H-J, Puelles L, Porteus MH, Grippo JF, Rubenstein JLR. 1993. The mouse dlx-2 (tes-1) gene
874 is expressed in spatially restricted domains of the forebrain, face and limbs in midgestation
875 mouse embryos. Review of. *Mechanisms of Development* **40**:129-140. doi: 10.1016/0925-
876 4773(93)90071-5
877 Burstyn-Cohen T, Kalcheim C. 2002. Association between the cell cycle and neural crest delamination
878 through specific regulation of g1/s transition. Review of. *Developmental Cell* **3**:383-395. doi:
879 10.1016/s1534-5807(02)00221-6
880 Burstyn-Cohen T, Stanleigh J, Sela-Donenfeld D, Kalcheim C. 2004. Canonical wnt activity regulates trunk
881 neural crest delamination linking bmp/noggin signaling with g1/s transition. Review of.
882 *Development* **131**:5327-5339. doi: 10.1242/dev.01424
883 Chai Y, Jiang X, Ito Y, Bringas P, Han J, Rowitch DH, Soriano P, McMahon AP, Sucov HM. 2000. Fate of the
884 mammalian cranial neural crest during tooth and mandibular morphogenesis. Review of.
885 *Development (Cambridge, England)* **127**:1671-1679. doi: 10.1242/dev.127.8.1671
886 Cheung M, Briscoe J. 2003. Neural crest development is regulated by the transcription factor sox9.
887 Review of. *Development* **130**:5681-5693. doi: 10.1242/dev.00808
888 Cheung M, Chaboissier M-C, Mynett A, Hirst E, Schedl A, Briscoe J. 2005. The transcriptional control of
889 trunk neural crest induction, survival, and delamination. Review of. *Developmental Cell* **8**:179-
890 192. doi: 10.1016/j.devcel.2004.12.010
891 Clay MR, Halloran MC. 2013. Rho activation is apically restricted by arhgap1 in neural crest cells and
892 drives epithelial-to-mesenchymal transition. Review of. *Development* **140**:3198-3209. doi:
893 10.1242/dev.095448
894 Dash S, Trainor PA. 2020. The development, patterning and evolution of neural crest cell differentiation
895 into cartilage and bone. Review of. *Bone* **137**:115409. doi: 10.1016/j.bone.2020.115409
896 Dong J, Hu Y, Fan X, Wu X, Mao Y, Hu B, Guo H, Wen L, Tang F. 2018. Single-cell rna-seq analysis unveils a
897 prevalent epithelial/mesenchymal hybrid state during mouse organogenesis. Review of.
898 *Genome Biology* **19**:31. doi: 10.1186/s13059-018-1416-2

899 Dongre A, Weinberg RA. 2019. New insights into the mechanisms of epithelial-mesenchymal transition
900 and implications for cancer. Review of. *Nature Reviews. Molecular Cell Biology* **20**:69-84. doi:
901 10.1038/s41580-018-0080-4
902 Dottori M, Gross MK, Labosky P, Goulding M. 2001. The winged-helix transcription factor foxd3
903 suppresses interneuron differentiation and promotes neural crest cell fate. Review of.
904 *Development* **128**:4127-4138. doi: 10.1242/dev.128.21.4127
905 Dunty WC, Jr., Kennedy MW, Chalamalasetty RB, Campbell K, Yamaguchi TP. 2014. Transcriptional
906 profiling of wnt3a mutants identifies sp transcription factors as essential effectors of the
907 wnt/beta-catenin pathway in neuromesodermal stem cells. Review of. *PLOS ONE* **9**:e87018. doi:
908 10.1371/journal.pone.0087018
909 Durkin ME, Avner MR, Huh C-G, Yuan B-Z, Thorgeirsson SS, Popescu NC. 2005. Dlc-1, a rho gtpase-
910 activating protein with tumor suppressor function, is essential for embryonic development.
911 Review of. *FEBS Letters* **579**:1191-1196. doi: 10.1016/j.febslet.2004.12.090
912 Echelard Y, Vassileva G, McMahon AP. 1994. Cis-acting regulatory sequences governing wnt-1
913 expression in the developing mouse cns. Review of. *Development* **120**:2213-2224. doi:
914 10.1242/dev.120.8.2213
915 Falcon KT, Watt KEN, Dash S, Zhao R, Sakai D, Moore EL, Fitriasari S, Childers M, Sardiu ME, Swanson S,
916 Tsuchiya D, Unruh J, Bugarinovic G, Li L, Shiang R, Achilleos A, Dixon J, Dixon MJ, Trainor PA.
917 2022. Dynamic regulation and requirement for ribosomal rna transcription during mammalian
918 development. Review of. *Proceedings of the National Academy of Sciences* **119**:e2116974119.
919 doi: 10.1073/pnas.2116974119
920 Golding JP, Trainor P, Krumlauf R, Gassmann M. 2000. Defects in pathfinding by cranial neural crest cells
921 in mice lacking the neuregulin receptor erbb4. Review of. *Nat Cell Biol* **2**:103-109. doi:
922 10.1038/35000058
923 Gonzalez VD, Samusik N, Chen TJ, Savig ES, Aghaeepour N, Quigley DA, Huang Y-W, Giangarrà V,
924 Borowsky AD, Hubbard NE, Chen S-Y, Han G, Ashworth A, Kipps TJ, Berek JS, Nolan GP, Fantl WJ.
925 2018. Commonly occurring cell subsets in high-grade serous ovarian tumors identified by single-
926 cell mass cytometry. Review of. *Cell Reports* **22**:1875-1888. doi: 10.1016/j.celrep.2018.01.053
927 Hafemeister C, Satija R. 2019. Normalization and variance stabilization of single-cell rna-seq data using
928 regularized negative binomial regression. Review of. *Genome Biology* **20**:296. doi:
929 10.1186/s13059-019-1874-1
930 Hari L, Miescher I, Shakhova O, Suter U, Chin L, Taketo M, Richardson WD, Kessaris N, Sommer L. 2012.
931 Temporal control of neural crest lineage generation by wnt/β-catenin signaling. Review of.
932 *Development (Cambridge, England)* **139**:2107-2117. doi: 10.1242/dev.073064
933 Hay ED. 1995. An overview of epithelio-mesenchymal transformation. Review of. *Acta Anatomica* **154**:8-
934 20. doi: 10.1159/000147748
935 Huang RY-J, Wong MK, Tan TZ, Kuay KT, Ng AHC, Chung VY, Chu Y-S, Matsumura N, Lai H-C, Lee YF, Sim
936 W-J, Chai C, Pietschmann E, Mori S, Low JJH, Choolani M, Thiery JP. 2013. An emt spectrum
937 defines an anoikis-resistant and spheroidogenic intermediate mesenchymal state that is
938 sensitive to e-cadherin restoration by a src-kinase inhibitor, saracatinib (azd0530). Review of.
939 *Cell Death & Disease* **4**:e915. doi: 10.1038/cddis.2013.442
940 Iyyanar PPR, Wu Z, Lan Y, Hu Y-C, Jiang R. 2022. Alx1 deficient mice recapitulate craniofacial phenotype
941 and reveal developmental basis of alx1-related frontonasal dysplasia. Review of. *Frontiers in Cell*
942 *and Developmental Biology* **10**.
943 Jiang X, Rowitch DH, Soriano P, McMahon AP, Sucov HM. 2000. Fate of the mammalian cardiac neural
944 crest. Review of. *Development* **127**:1607-1616. doi: 10.1242/dev.127.8.1607
945 Karacosta LG, Anchang B, Ignatiadis N, Kimmey SC, Benson JA, Shrager JB, Tibshirani R, Bendall SC,
946 Plevritis SK. 2019. Mapping lung cancer epithelial-mesenchymal transition states and

947 trajectories with single-cell resolution. Review of. *Nature Communications* **10**:5587. doi:
948 10.1038/s41467-019-13441-6
949 Kim TY, Healy KD, Der CJ, Sciaky N, Bang Y-J, Juliano RL. 2008. Effects of structure of rho gtpase-
950 activating protein dlc-1 on cell morphology and migration*. Review of. *Journal of Biological*
951 *Chemistry* **283**:32762-32770. doi: 10.1074/jbc.M800617200
952 Kishi JY, Lapan SW, Beliveau BJ, West ER, Zhu A, Sasaki HM, Saka SK, Wang Y, Cepko CL, Yin P. 2019.
953 Saber amplifies fish: Enhanced multiplexed imaging of rna and DNA in cells and tissues. Review
954 of. *Nature Methods* **16**:533-544. doi: 10.1038/s41592-019-0404-0
955 Kobayashi GS, Musso CM, Moreira DdP, Pontillo-Guimarães G, Hsia GSP, Caires-Júnior LC, Goulart E,
956 Passos-Bueno MR. 2020. Recapitulation of neural crest specification and emt via induction from
957 neural plate border-like cells. Review of. *Stem Cell Reports* **15**:776-788. doi:
958 10.1016/j.stemcr.2020.07.023
959 Kumar SU, Kumar DT, Siva R, Doss CGP, Zayed H. 2019. Integrative bioinformatics approaches to map
960 potential novel genes and pathways involved in ovarian cancer. Review of. *Frontiers in*
961 *Bioengineering and Biotechnology* **7**:391. doi: 10.3389/fbioe.2019.00391
962 Lee RTH, Nagai H, Nakaya Y, Sheng G, Trainor PA, Weston JA, Thiery JP. 2013. Cell delamination in the
963 mesencephalic neural fold and its implication for the origin of ectomesenchyme. Review of.
964 *Development (Cambridge, England)* **140**:4890-4902. doi: 10.1242/dev.094680
965 Li J, Chen F, Epstein JA. 2000. Neural crest expression of cre recombinase directed by the proximal pax3
966 promoter in transgenic mice. Review of. *genesis* **26**:162-164. doi: 10.1002/(SICI)1526-
967 968X(200002)26:2<162::AID-GENE21>3.0.CO;2-R
968 Lièvre CSL, Douarin NML. 1975. Mesenchymal derivatives of the neural crest: Analysis of chimaeric quail
969 and chick embryos. Review of. *Development* **34**:125-154. doi: 10.1242/dev.34.1.125
970 Liu JA, Rao Y, Cheung MPL, Hui M-N, Wu M-H, Chan L-K, Ng IO-L, Niu B, Cheah KSE, Sharma R, Hodgson L,
971 Cheung M. 2017. Asymmetric localization of dlc1 defines avian trunk neural crest polarity for
972 directional delamination and migration. Review of. *Nature Communications* **8**:1185. doi:
973 10.1038/s41467-017-01107-0
974 Lumb R, Wiszniak S, Kabbara S, Scherer M, Harvey N, Schwarz Q. 2014. Neuropilins define distinct
975 populations of neural crest cells. Review of. *Neural Development* **9**:24. doi: 10.1186/1749-8104-
976 9-24
977 Mandalos N, Rhinn M, Granchi Z, Karampelas I, Mitsiadis T, Economides AN, Dollé P, Remboutsika E.
978 2014. Sox2 acts as a rheostat of epithelial to mesenchymal transition during neural crest
979 development. Review of. *Frontiers in Physiology* **5**:345. doi: 10.3389/fphys.2014.00345
980 Matsuuchi L, Naus CC. 2013. Gap junction proteins on the move: Connexins, the cytoskeleton and
981 migration. Review of. *Biochimica et Biophysica Acta (BBA) - Biomembranes* **1828**:94-108. doi:
982 10.1016/j.bbamem.2012.05.014
983 McKeown SJ, Lee VM, Bronner-Fraser M, Newgreen DF, Farlie PG. 2005. Sox10 overexpression induces
984 neural crest-like cells from all dorsoventral levels of the neural tube but inhibits differentiation.
985 Review of. *Developmental Dynamics* **233**:430-444. doi: 10.1002/dvdy.20341
986 McKinney MC, Fukatsu K, Morrison J, McLennan R, Bronner ME, Kulesa PM. 2013. Evidence for dynamic
987 rearrangements but lack of fate or position restrictions in premigratory avian trunk neural crest.
988 Review of. *Development (Cambridge, England)* **140**:820-830. doi: 10.1242/dev.083725
989 Muñoz WA, Trainor PA. 2019. Mouse embryo culture for the study of neural crest cells. Review of.
990 *Methods in Molecular Biology (Clifton, N.J.)* **1976**:107-119. doi: 10.1007/978-1-4939-9412-0_9
991 Murdoch B, DelConte C, García-Castro MI. 2012. Pax7 lineage contributions to the mammalian neural
992 crest. Review of. *PLOS ONE* **7**:e41089. doi: 10.1371/journal.pone.0041089

993 Parr BA, Shea MJ, Vassileva G, McMahon AP. 1993. Mouse wnt genes exhibit discrete domains of
994 expression in the early embryonic cns and limb buds. Review of. *Development* **119**:247-261. doi:
995 10.1242/dev.119.1.247
996 Pastushenko I, Brisebarre A, Sifrim A, Fioramonti M, Revenco T, Boumahdi S, Van Keymeulen A, Brown
997 D, Moers V, Lemaire S, De Clercq S, Minguijón E, Balsat C, Sokolow Y, Dubois C, De Cock F,
998 Scozzaro S, Sopena F, Lanas A, D'Haene N, Salmon I, Marine J-C, Voet T, Sotiropoulou PA,
999 Blanpain C. 2018. Identification of the tumour transition states occurring during emt. Review of.
1000 *Nature* **556**:463-468. doi: 10.1038/s41586-018-0040-3
1001 Piccand J, Meunier A, Merle C, Jia Z, Barnier J-V, Gradwohl G. 2014. Pak3 promotes cell cycle exit and
1002 differentiation of β-cells in the embryonic pancreas and is necessary to maintain glucose
1003 homeostasis in adult mice. Review of. *Diabetes* **63**:203-215. doi: 10.2337/db13-0384
1004 Popoff MR, Geny B. 2009. Multifaceted role of rho, rac, cdc42 and ras in intercellular junctions, lessons
1005 from toxins. Review of. *Biochimica et Biophysica Acta (BBA) - Biomembranes* **1788**:797-812. doi:
1006 10.1016/j.bbamem.2009.01.011
1007 Puram SV, Tirosh I, Parikh AS, Patel AP, Yizhak K, Gillespie S, Rodman C, Luo CL, Mroz EA, Emerick KS,
1008 Deschler DG, Varvares MA, Mylvaganam R, Rozenblatt-Rosen O, Rocco JW, Faquin WC, Lin DT,
1009 Regev A, Bernstein BE. 2017. Single-cell transcriptomic analysis of primary and metastatic tumor
1010 ecosystems in head and neck cancer. Review of. *Cell* **171**:1611-1624.e1624. doi:
1011 10.1016/j.cell.2017.10.044
1012 Radisky ES, Radisky DC. 2010. Matrix metalloproteinase-induced epithelial-mesenchymal transition in
1013 breast cancer. Review of. *Journal of Mammary Gland Biology and Neoplasia* **15**:201-212. doi:
1014 10.1007/s10911-010-9177-x
1015 Remboutsika E, Elkouris M, Iulianella A, Andoniadou CL, Poulou M, Mitsiadis TA, Trainor PA, Lovell-
1016 Badge R. 2011. Flexibility of neural stem cells. Review of. *Frontiers in Physiology* **2**:16. doi:
1017 10.3389/fphys.2011.00016
1018 Sabbir MG, Wigle N, Loewen S, Gu Y, Buse C, Hicks GG, Mowat MR. 2010. Identification and
1019 characterization of dlc1 isoforms in the mouse and study of the biological function of a single
1020 gene trapped isoform. Review of. *BMC Biology* **8**:17. doi: 10.1186/1741-7007-8-17
1021 Sakai D, Trainor PA. 2014. Gene transfer techniques in whole embryo cultured post-implantation mouse
1022 embryos. Review of. *Methods Mol Biol* **1092**:227-234. doi: 10.1007/978-1-60327-292-6_15
1023 Sakai D, Trainor PA. 2016. Face off against ros: Tcof1/treacle safeguards neuroepithelial cells and
1024 progenitor neural crest cells from oxidative stress during craniofacial development. Review of.
1025 *Dev Growth Differ* **58**:577-585. doi: 10.1111/dgd.12305
1026 Sandell LL, Trainor PA. 2006. Neural crest cell plasticity. In *Neural crest induction and differentiation*,
1027 edited by Saint-Jeannet J-P, 78-95. Boston, MA: Springer US.
1028 Sauka-Spengler T, Bronner-Fraser M. 2008. A gene regulatory network orchestrates neural crest
1029 formation. Review of. *Nature Reviews. Molecular Cell Biology* **9**:557-568. doi: 10.1038/nrm2428
1030 Schindelin J, Arganda-Carreras I, Frise E, Kaynig V, Longair M, Pietzsch T, Preibisch S, Rueden C, Saalfeld
1031 S, Schmid B, Tinevez J-Y, White DJ, Hartenstein V, Eliceiri K, Tomancak P, Cardona A. 2012. Fiji:
1032 An open-source platform for biological-image analysis. Review of. *Nature Methods* **9**:676-682.
1033 doi: 10.1038/nmeth.2019
1034 Schorle H, Meier P, Buchert M, Jaenisch R, Mitchell PJ. 1996. Transcription factor ap-2 essential for
1035 cranial closure and craniofacial development. Review of. *Nature* **381**:235-238. doi:
1036 10.1038/381235a0
1037 Soldatov R, Kaucka M, Kastriti ME, Petersen J, Chontorotzea T, Englmaier L, Akkuratova N, Yang Y, Häring
1038 M, Dyachuk V, Bock C, Farlik M, Piacentino ML, Boismoreau F, Hilscher MM, Yokota C, Qian X,
1039 Nilsson M, Bronner ME, Croci L, Hsiao W-Y, Guertin DA, Brunet J-F, Consalez GG, Ernfors P, Fried

K, Kharchenko PV, Adameyko I. 2019. Spatiotemporal structure of cell fate decisions in murine neural crest. Review of. *Science (New York, N.Y.)* **364**. doi: 10.1126/science.aas9536

Soo K, O'Rourke MP, Khoo P-L, Steiner KA, Wong N, Behringer RR, Tam PPL. 2002. Twist function is required for the morphogenesis of the cephalic neural tube and the differentiation of the cranial neural crest cells in the mouse embryo. Review of. *Developmental Biology* **247**:251-270. doi: 10.1006/dbio.2002.0699

Stringer C, Wang T, Michaelos M, Pachitariu M. 2021. Cellpose: A generalist algorithm for cellular segmentation. Review of. *Nature Methods* **18**:100-106. doi: 10.1038/s41592-020-01018-x

Stuart T, Butler A, Hoffman P, Hafemeister C, Papalexi E, Mauck WM, 3rd, Hao Y, Stoeckius M, Smibert P, Satija R. 2019. Comprehensive integration of single-cell data. Review of. *Cell* **177**:1888-1902 e1821. doi: 10.1016/j.cell.2019.05.031

Terry S, Nie M, Matter K, Balda MS. 2010. Rho signaling and tight junction functions. Review of. *Physiology* **25**:16-26. doi: 10.1152/physiol.00034.2009

Thevenaz P, Ruttimann UE, Unser M. 1998. A pyramid approach to subpixel registration based on intensity. Review of. *IEEE Transactions on Image Processing* **7**:27-41. doi: 10.1109/83.650848

Théveneau E, Duband J-L, Altabef M. 2007. Ets-1 confers cranial features on neural crest delamination. Review of. *PLOS ONE* **2**:e1142. doi: 10.1371/journal.pone.0001142

Trainor P, Krumlauf R. 2000a. Plasticity in mouse neural crest cells reveals a new patterning role for cranial mesoderm. Review of. *Nat Cell Biol* **2**:96-102. doi: 10.1038/35000051

Trainor PA. 2005. Specification of neural crest cell formation and migration in mouse embryos. Review of. *Seminars in Cell & Developmental Biology* **16**:683-693. doi: 10.1016/j.semcdb.2005.06.007

Trainor PA, Krumlauf R. 2000b. Patterning the cranial neural crest: Hindbrain segmentation and hox gene plasticity. Review of. *Nat Rev Neurosci* **1**:116-124. doi: 10.1038/35039056

Trainor PA, Krumlauf R. 2001. Hox genes, neural crest cells and branchial arch patterning. Review of. *Curr Opin Cell Biol* **13**:698-705. doi: 10.1016/s0955-0674(00)00273-8

Van de Putte T, Maruhashi M, Francis A, Nelles L, Kondoh H, Huylebroeck D, Higashi Y. 2003. Mice lacking zfhx1b, the gene that codes for smad-interacting protein-1, reveal a role for multiple neural crest cell defects in the etiology of hirschsprung disease-mental retardation syndrome. Review of. *American Journal of Human Genetics* **72**:465-470. doi: 10.1086/346092

Varberg JM, Unruh JR, Bestul AJ, Khan AA, Jaspersen SL. 2022. Quantitative analysis of nuclear pore complex organization in schizosaccharomyces pombe. Review of. *Life Science Alliance* **5**:e202201423. doi: 10.26508/lsa.202201423

Wakamatsu Y, Endo Y, Osumi N, Weston JA. 2004. Multiple roles of sox2, an hmg-box transcription factor in avian neural crest development. Review of. *Developmental Dynamics* **229**:74-86. doi: 10.1002/dvdy.10498

Watt KEN, Trainor PA. 2014. Chapter 17 - neurocristopathies: The etiology and pathogenesis of disorders arising from defects in neural crest cell development. In *Neural crest cells*, edited by Trainor PA, 361-394. Boston: Academic Press.

Weston JA. 1983. Embryonic development: The neural crest. Nicole le douarin. Cambridge university press, new york, 1983. Xii, 260 pp., illus. $65. Developmental and cell biology series, 12. Review of. *Science* **220**:1372-1372. doi: 10.1126/science.220.4604.1372

Wood HB, Episkopou V. 1999. Comparative expression of the mouse sox1, sox2 and sox3 genes from pre-gastrulation to early somite stages. Review of. *Mechanisms of Development* **86**:197-201. doi: 10.1016/s0925-4773(99)00116-1

Yang J, Antin P, Berx G, Blanpain C, Brabletz T, Bronner M, Campbell K, Cano A, Casanova J, Christofori G, Dedhar S, Derynck R, Ford HL, Fuxe J, Garcia de Herreros A, Goodall GJ, Hadjantonakis AK, Huang RYJ, Kalcheim C, Kalluri R, Kang Y, Khew-Goodall Y, Levine H, Liu J, Longmore GD, Mani SA, Massague J, Mayor R, McClay D, Mostov KE, Newgreen DF, Nieto MA, Puisieux A, Runyan R,

1088 Savagner P, Stanger B, Stemmler MP, Takahashi Y, Takeichi M, Theveneau E, Thiery JP,
1089 Thompson EW, Weinberg RA, Williams ED, Xing J, Zhou BP, Sheng G, Association EMTI. 2020a.
1090 Guidelines and definitions for research on epithelial-mesenchymal transition. Review of. *Nat Rev*
1091 *Mol Cell Biol* **21**:341-352. doi: 10.1038/s41580-020-0237-9
1092 Yang X, Hu F, Liu JA, Yu S, Cheung MPL, Liu X, Ng IO, Guan XY, Wong KKW, Sharma R, Lung HL, Jiao Y, Lee
1093 LTO, Cheung M. 2020b. Nuclear dlc1 exerts oncogenic function through association with foxk1
1094 for cooperative activation of mmp9 expression in melanoma. Review of. *Oncogene* **39**:4061-
1095 4076. doi: 10.1038/s41388-020-1274-8
1096 Yu M, Bardia A, Wittner BS, Stott SL, Smas ME, Ting DT, Isakoff SJ, Ciciliano JC, Wells MN, Shah AM,
1097 Concannon KF, Donaldson MC, Sequist LV, Brachtel E, Sgroi D, Baselga J, Ramaswamy S, Toner
1098 M, Haber DA, Maheswaran S. 2013. Circulating breast tumor cells exhibit dynamic changes in
1099 epithelial and mesenchymal composition. Review of. *Science (New York, N.Y.)* **339**:580-584. doi:
1100 10.1126/science.1228522
1101 Zhao R, Trainor PA. 2023. Epithelial to mesenchymal transition during mammalian neural crest cell
1102 delamination. Review of. *Seminars in Cell & Developmental Biology* **138**:54-67. doi:
1103 10.1016/j.semcdb.2022.02.018

1104

1105

1106 **Figures and figure legends**

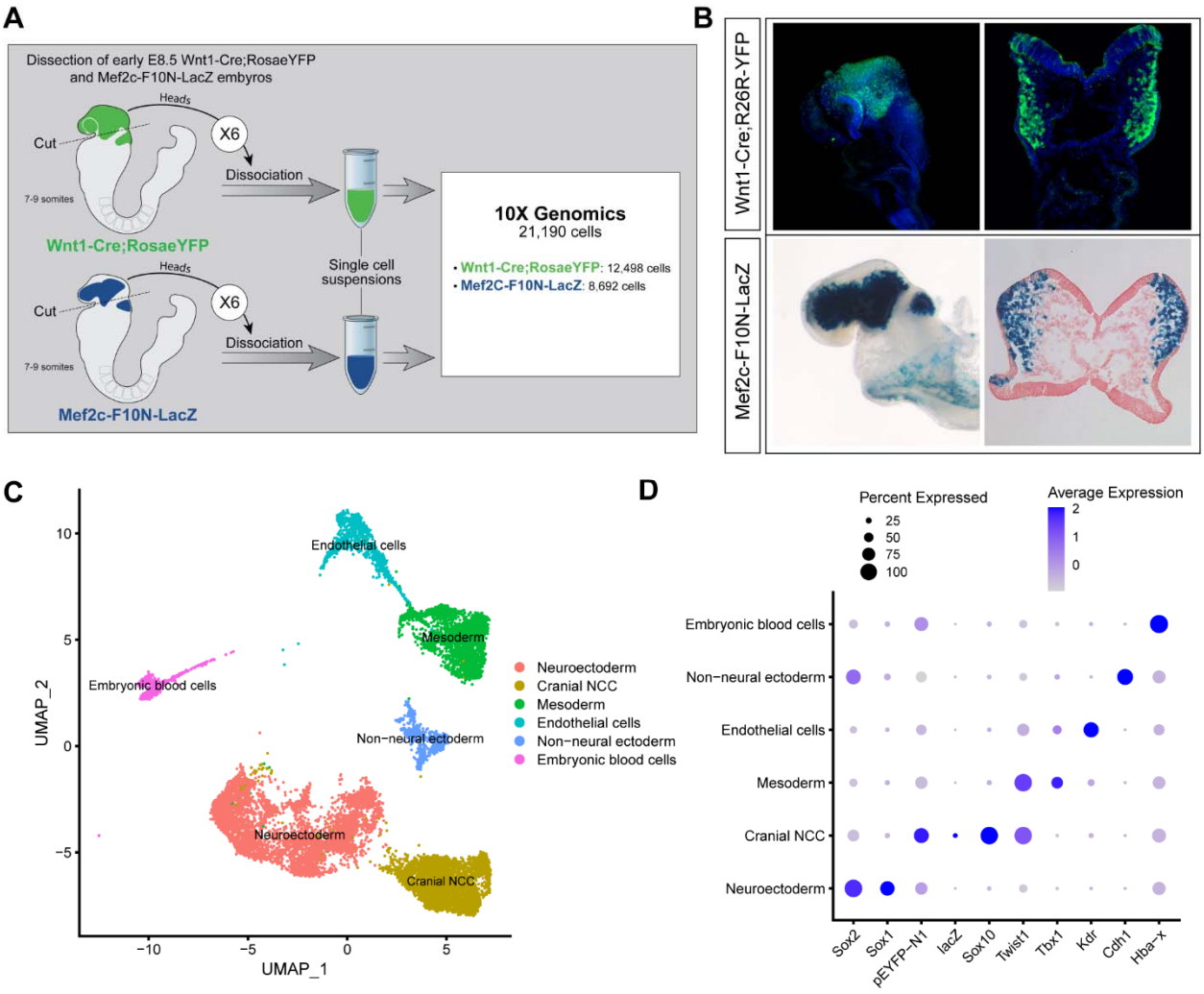

1107

1108 **Figure 1.** Single-cell RNA seq analysis of mouse early E8.5 cranial tissues. (A) Schematic of
1109 experimental design. *Wnt1-Cre;RosaeYFP* and *Mef2c-F10N-LacZ* embryos with between 7-9
1110 somites (6 each) were dissected and cranial tissues anterior to rhombomere 3 were collected.
1111 Tissues were dissociated into single cell suspensions before being processed through the 10X
1112 Genomics pipeline. The final dataset used for analysis consisted of 21,190 cells (12,498 cells
1113 from *Wnt1-Cre;RosaeYFP* and 8,692 from *Mef2c-F10N-LacZ*) and 29,041 genes. (B) YFP and LacZ
1114 staining of E8.5 *Wnt1-Cre;RosaeYFP* and *Mef2c-F10N-LacZ* embryos and 10um cranial
1115 transverse sections. YFP (green) labels cells located in the dorsal neuroepithelium and their
1116 lineages. As a result, both premigratory and migratory NCC are marked by YFP expression. LacZ
1117 (blue) labels migratory NCC. (C) Uniform Manifold Approximation and Projection (UMAP) and
1118 clustering of 6 major tissue types in the cranial region of E8.5 mouse embryos: cranial NCC,
1119 neuroectoderm, non-neural ectoderm, mesoderm, endothelial cells, and embryonic blood cells.
1120 (D) Dotplot showing the expression of tissue specific markers used for cluster identification. Dot

size indicates the percentage of cells in each corresponding cluster (y-axis) that expresses a specific gene (x-axis). Dot color intensity indicates the average expression level of a specific gene in a cell cluster.

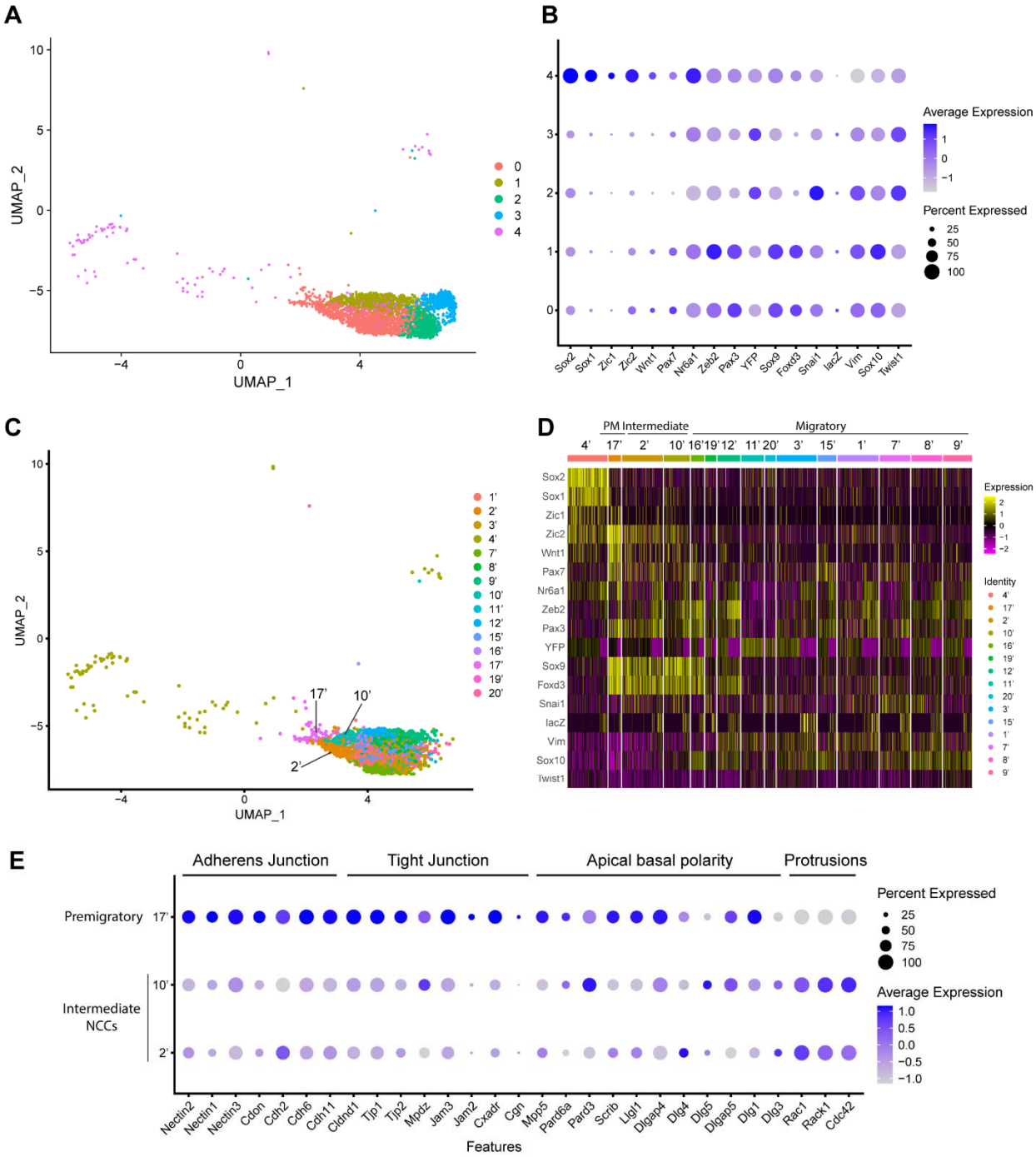

Figure 2. Expression of NCC development related genes and EMT functional genes identifies NCC EMT intermediate populations. (A) UMAP and re-clustering of the cranial NCC cluster into 5 smaller subclusters at a resolution of 0.26. (B) Dotplot showing the expression of NCC

development related genes in 5 cranial NCC subclusters. (C) UMAP and re-clustering of the early migratory NCC subclusters 0, 1 and 4 into smaller subclusters at a resolution of 2.0. (D) Heatmap showing the expression of NCC development related genes in the smaller early migratory NCC subclusters at a resolution of 2.0 shown in (C). High levels of expression are indicated in yellow, and low levels of expression are indicated in pink. Based on the gene expression profile of each subcluster, subcluster 17’ was determined to be premigratory NCC; subcluster 2’ and 10’ are EMT intermediate NCC; the remaining subclusters are migratory NCC. (E) Dotplot showing the expression of EMT functional genes in premigratory NCC subcluster 17’ and intermediate NCC subclusters 2’ and 10’. EMT intermediate NCC display reduced expression of adherens junction, tight junction and apical basal polarity genes compared to premigratory NCC, whereas protrusion related genes are upregulated in intermediate NCC.

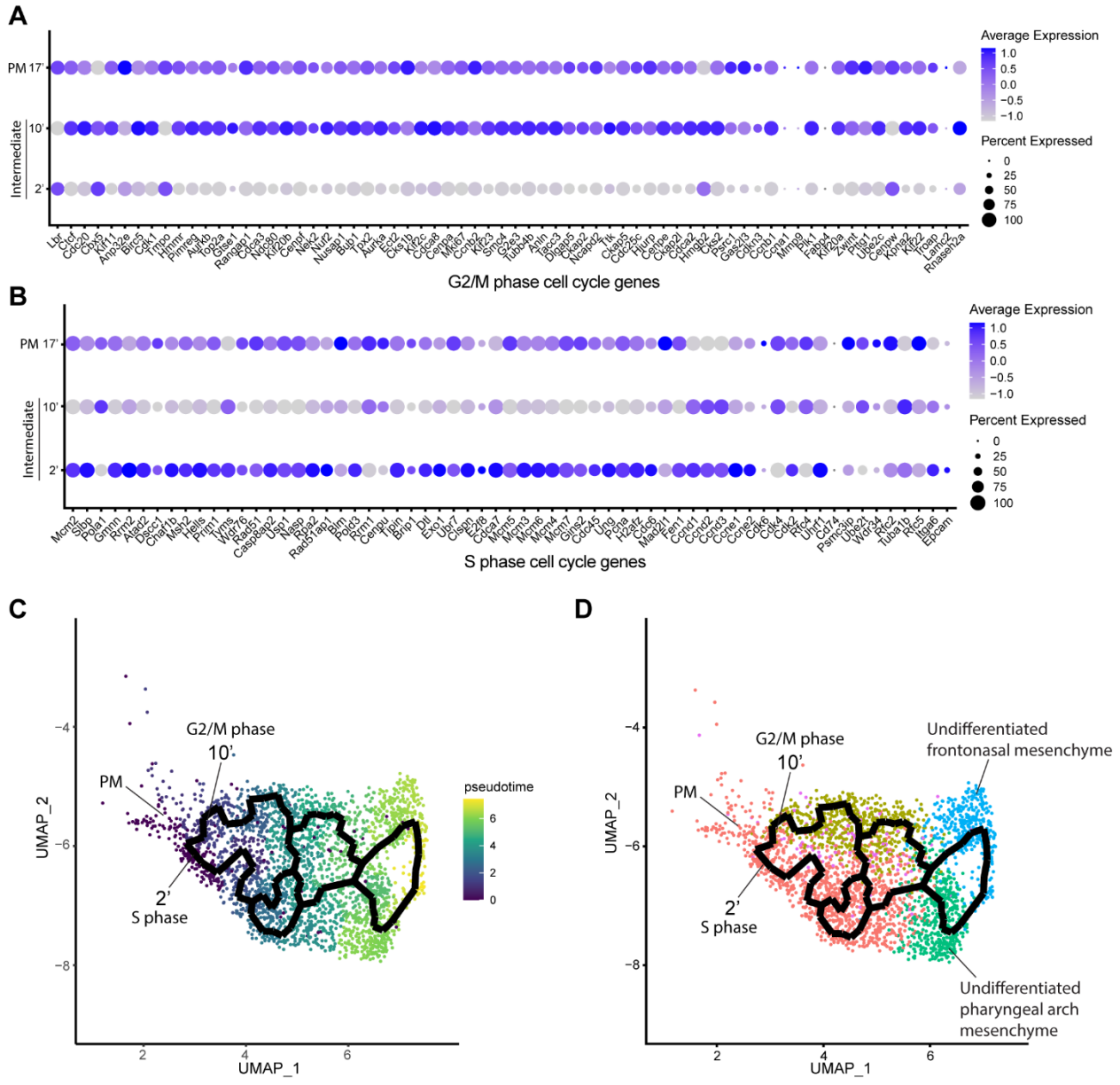

1140 **Figure 3.** Mouse cranial NCC delaminate in S phase or G2/M phase cell cycle independently. (A)
1141 Dotplot showing the expression of G2/M phase cell cycle genes in premigratory NCC (PM) and
1142 EMT intermediate NCC. G2/M phase cell cycle genes are expressed in PM and intermediate
1143 subcluster 10' cells. (B) Dotplot showing the expression of S phase cell cycle genes in PM and
1144 EMT intermediate NCC. S phase cell cycle genes are expressed in PM and intermediate
1145 subcluster 2' cells. (C) Pseudotime analysis of the cranial NCC cluster reveals the temporal
1146 relationship between intermediate NCC subcluster 2' and 10'. Dark color indicates early NCC
1147 development, and light color indicates later NCC development. PM and intermediate NCC
1148 subclusters represent the earliest developmental timepoints among all cranial NCC. (D)
1149 Trajectory analysis of the cranial NCC cluster reveals lineage/fate relationship between PM and
1150 intermediate NCC subcluster 2' and 10'. Two intermediate NCC subclusters develop
1151 simultaneously and independently from premigratory NCC. Apart from their cell cycle status,
1152 early migratory NCC formed from the different intermediate subclusters are transcriptionally
1153 indistinguishable.

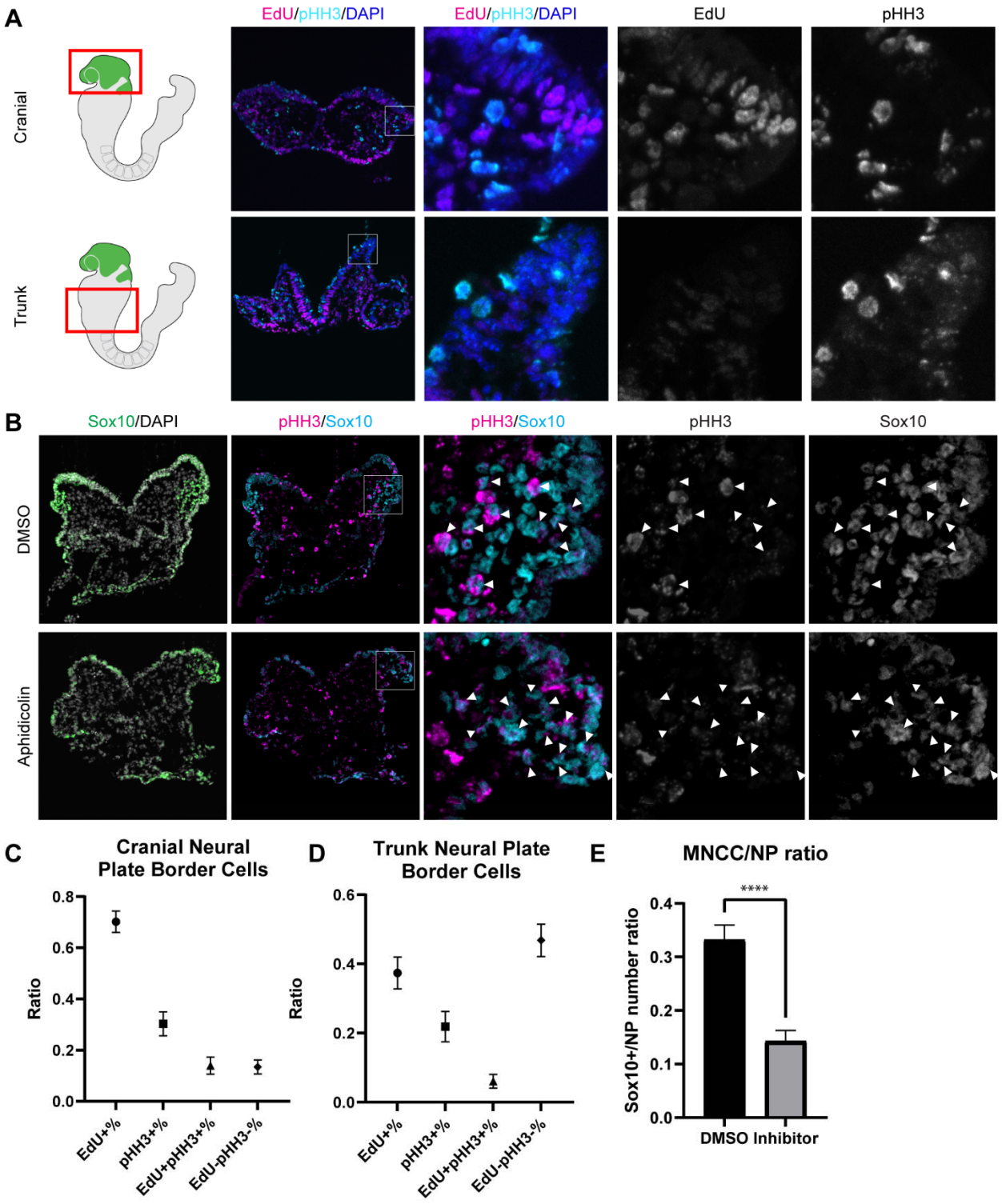

1154

1155 **Figure 4.** Cell cycle regulation plays an important role in mouse cranial NCC delamination and
1156 EMT. (A) Cell cycle marker staining of early E8.5 mouse embryonic cranial and trunk tissues
1157 reveals differences in cell cycle status between cranial delaminating premigratory NCC and
1158 trunk neural plate border cells. EdU (magenta) and pHH3 (cyan) staining were performed on

10um transverse sections of early E8.5 (5-7 somites) *Wnt1-Cre;RosaeYFP* mouse embryo cranial and trunk tissues. (B) E8.0 CD1 mouse embryos treated with Aphidicolin exhibit reduced migratory NCC that primarily express pHH3. Cranial sections of treated embryos were stained with Sox10, EdU and pHH3 (magenta) and arrowheads indicate migratory NCC expressing pHH3. Most remaining migratory NCC in Aphidicolin treated samples express pHH3. In contrast, a small proportion of migratory NCC in control DMSO treated samples express pHH3. (C) Cell cycle staining quantification of delaminating premigratory NCC in the cranial neural plate border shows that most cells express cell cycle markers. Staining and quantification were performed on delaminating premigratory NCC in the cranial neural plate border of 5-7 somite *Wnt1-Cre;RosaeYFP* mouse embryos (n=3). The neural plate border region was manually selected in the most dorsolateral domain of the neural plate. EdU+%=the percentage of EdU positive cells within eYFP positive delaminating premigratory NCC in the selected neural plate border domain. pHH3+%= the percentage of pHH3 positive cells within eYFP positive delaminating premigratory NCC. EdU+pHH3+%= the percentage of EdU and pHH3 double positive cells within eYFP positive delaminating premigratory NCC. EdU-pHH3-%= the percentage of EdU and pHH3 double negative cells within eYFP positive delaminating premigratory NCC. (D) Cell cycle staining quantification of trunk neural plate border cells shows that a significant proportion of cells do not express any cell cycle markers. Staining and quantification were performed on trunk neural plate border cells of 5-7 somite *Wnt1-Cre;RosaeYFP* mouse embryos (n=3). The neural plate border region was manually selected in the most dorsolateral domain of the neural plate. EdU+%=the percentage of EdU positive cells within DAPI positive neural plate border cells at the trunk axial level. pHH3+%= the percentage of pHH3 positive cells within DAPI positive trunk neural plate border cells. EdU+pHH3+%= the percentage of EdU and pHH3 double positive cells within DAPI positive trunk neural plate border cells. EdU-pHH3-%= the percentage of EdU and pHH3 double negative cells within DAPI positive trunk neural plate border cells. (E) Quantification of Sox10 expressing migratory NCC upon Aphidicolin and control treatment reveals fewer cranial migratory NCC in Aphidicolin treated embryos. Sox10 staining and quantification were performed on cranial sections of 4-6 somite CD1 mouse embryos post treatment (n=3 per treatment; ****$p<0.0001$). For quantification, we calculated the ratio of Sox10 positive migratory NCC over DAPI positive neural plate/neuroepithelial cells.

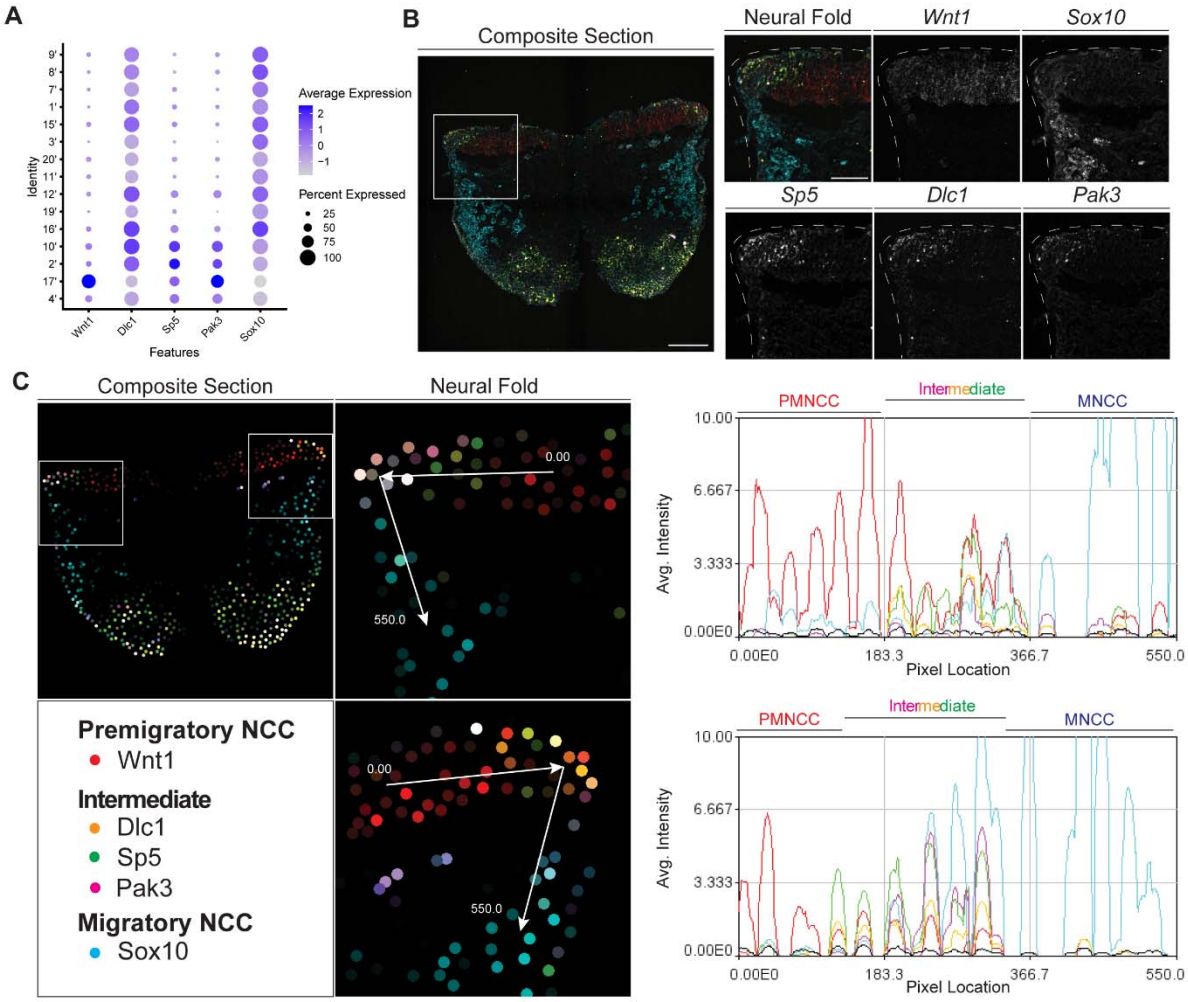

Figure 5. SABER-FISH of EMT intermediate stage markers pinpoints the location of EMT intermediate NCC within the dorsal most region of the neural fold. (A) Dotplot showing the expression of selected EMT intermediate NCC markers in early migratory NCC subclusters (resolution 2.0). (B) SABER-FISH staining of premigratory, EMT intermediate stage and migratory NCC marker genes on the same section. Higher magnification insets of the left side neural fold (box) showing that *Wnt1* is expressed in the neuroepithelium and *Sox10* is expressed in migratory NCC populating the underlying mesenchyme. *Dlc1*, *Sp5* and *Pak3* are expressed in the dorsolateral most region of the neuroepithelium. (C) 2D map showing the number of transcripts per cell, calculated from the SABER-FISH staining. To evaluate the expression of each gene within and across tissues, a polyline kymograph was generated along

1201 the track indicated by the arrows at a width of 100 pixels. The polyline kymograph can be seen
1202 to the right of each neural fold map it depicts. At the beginning of the track, *Wnt1* expression is
1203 highest, demarcating the dorsal lateral domain of the neuroepithelium. Towards the middle of
1204 the track, at the location of the most dorsolateral region of the neuroepithelium, *Wnt1* is
1205 expressed along with the intermediate stage markers *Dlc1, Sp5* and *Pak3*. As the track
1206 progresses to just outside of the neuroepithelium, *Sox10* expression appears and increases as
1207 the track continues through the migratory NCC population.

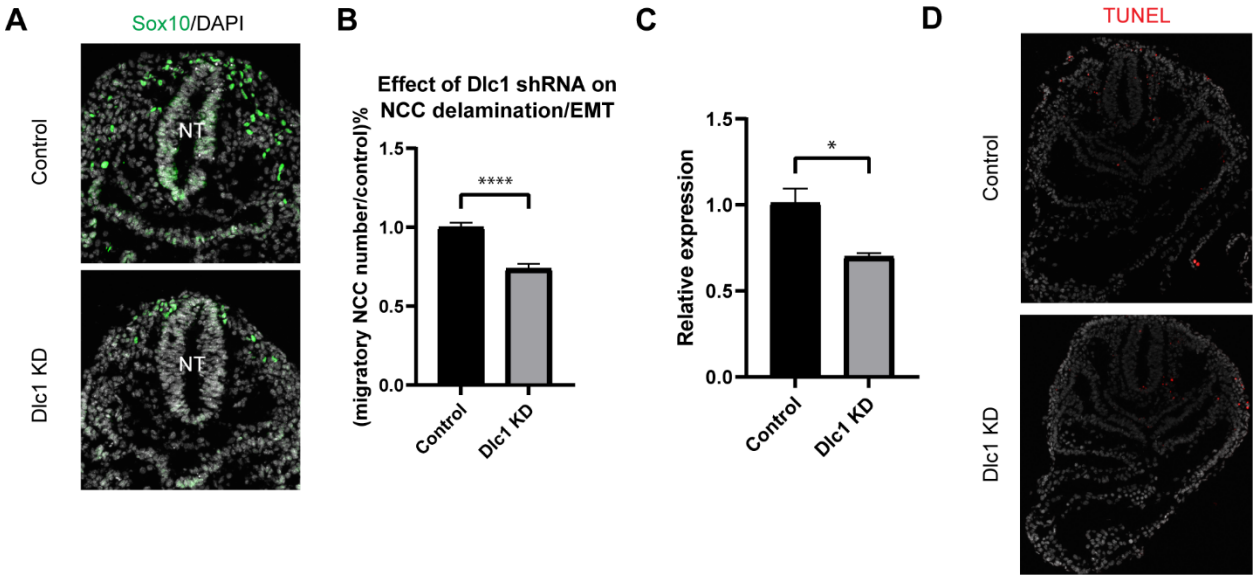

1208

1209 **Figure 6.** Dlc1 plays a regulatory role in mouse cranial NCC EMT and delamination. (A) Sox10
1210 immunostaining was performed on cranial sections of E8.5 control and *Dlc1* knockdown mouse
1211 embryos. (B) *Dlc1* knockdown significantly reduced the number of migratory NCC compared to
1212 the control. The number of Sox10+ migratory NCC was quantified in control (n=4) and all *Dlc1*
1213 knockdown (n=12) embryos. All datapoints in *Dlc1* knockdown samples were normalized to the
1214 control samples. ****$p<0.0001$. (C) *Dlc1* shRNA-based lentiviruses achieved an average of 30%
1215 reduction of *Dlc1* expression in all *Dlc1* knockdown embryos based on qRT-PCR analysis.
1216 *$p<0.05$. (D) TUNEL staining showed minimal cell death in *Dlc1* knockdown samples.

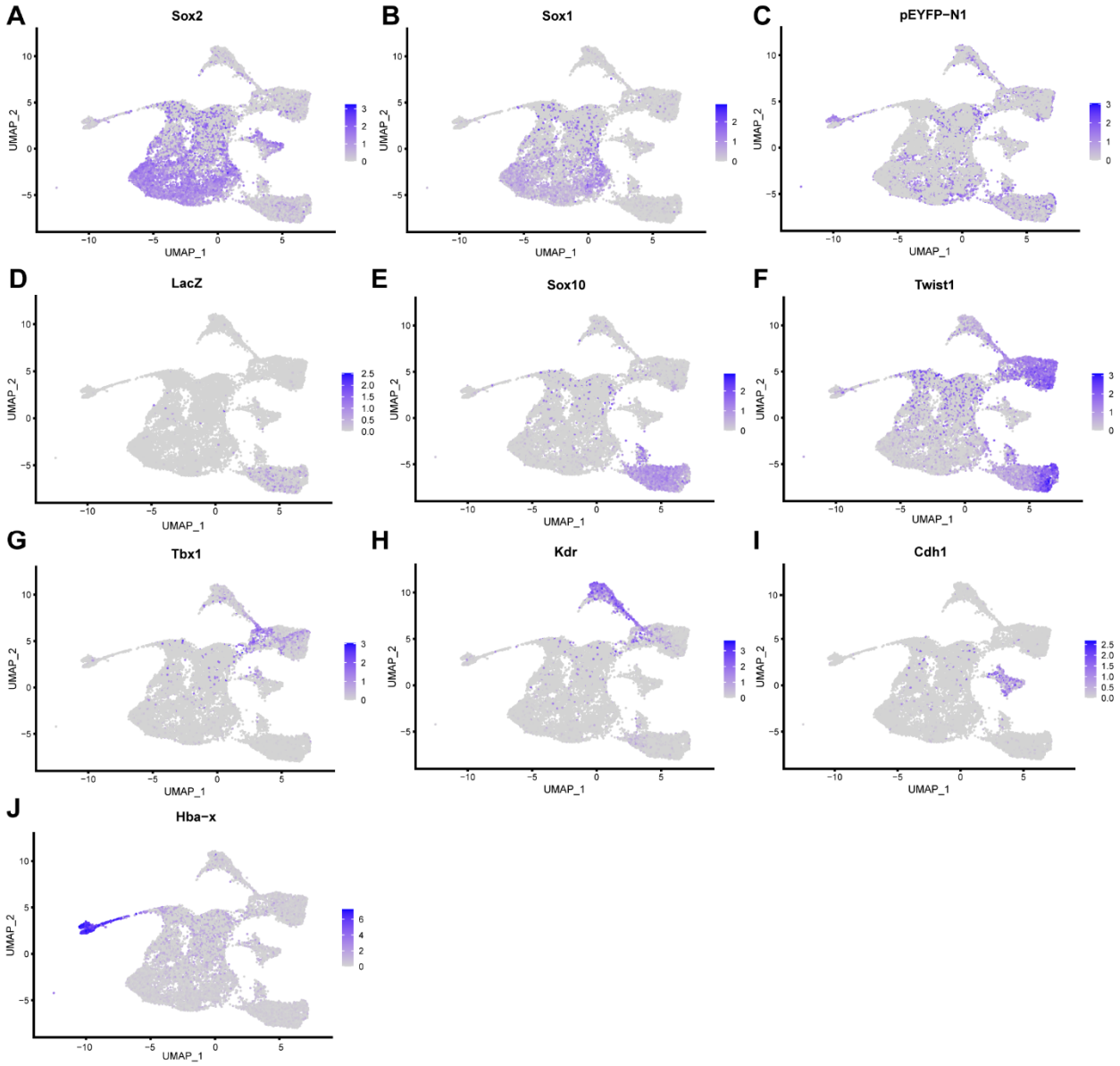

Figure 1-figure supplement 1. Expression of tissue specific marker genes that identify 6 major cell type clusters in early E8.5 mouse embryonic cranial tissues. FeaturePlots that show the expression of (A) *Sox2*, neuroectoderm marker; (B) *Sox1*, neuroectoderm marker; (C) *eYFP*, premigratory and migratory NCC marker; (D) *LacZ*, migratory NCC marker; (E) *Sox10*, migratory NCC marker; (F) *Twist1*, NCC and mesoderm marker; (G) *Tbx1*, mesoderm marker; (H) *Kdr*, endothelial cell marker; (I) *Cdh1*, non-neural ectoderm marker; (J) *Hba-x*, embryonic blood cell marker.

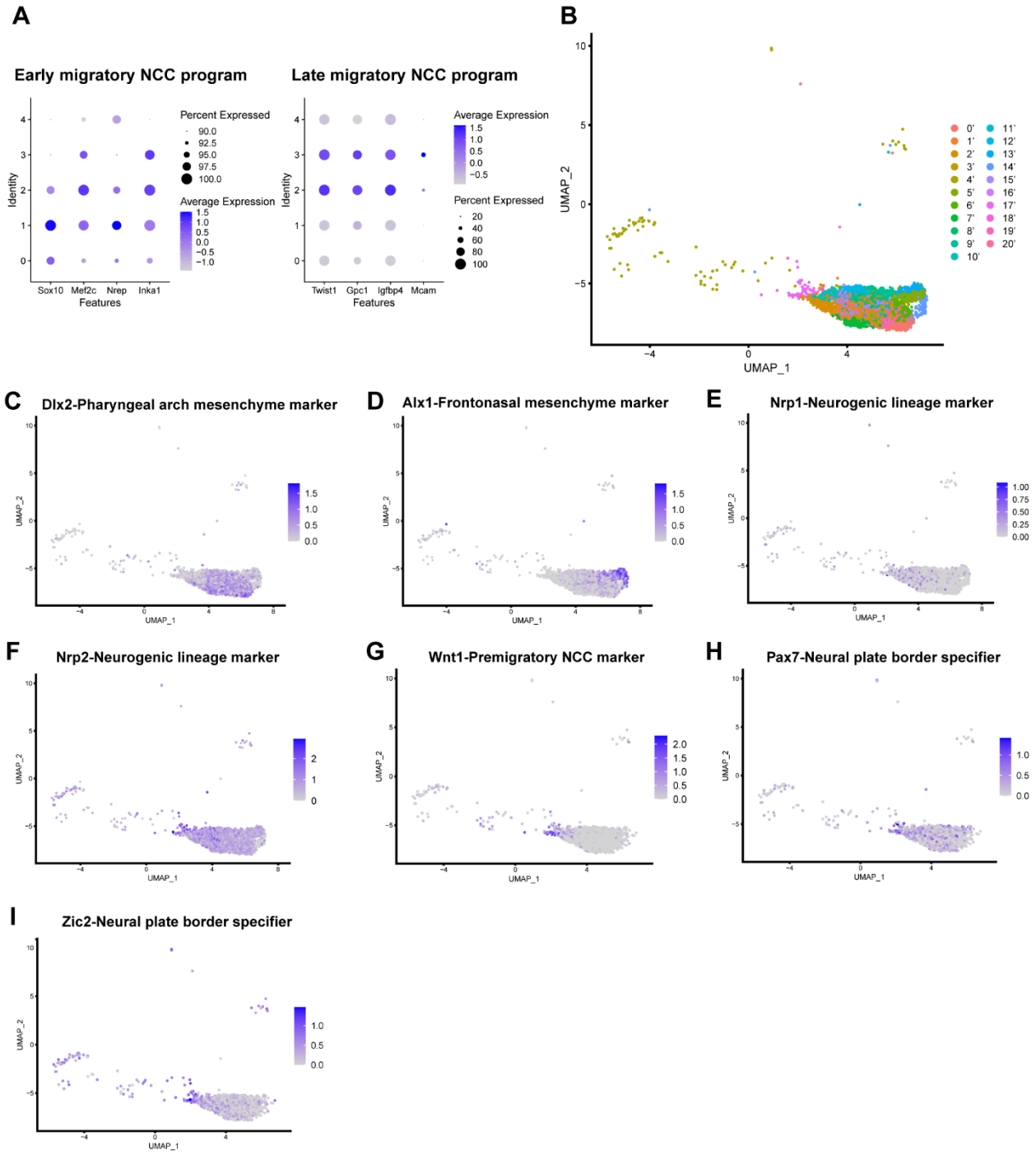

Figure 2-figure supplement 1. Additional gene expressions that support the identity of cranial NCC subclusters at 0.26 and 2.0 resolutions. (A) Expression of NCC development program genes (Soldatov et al., 2019) confirms NCC subcluster 0 and 1 as early migratory NCC and subcluster 2 and 3 as late migratory NCC. Dotplots showing the expression of early and late NCC program genes in 5 NCC subclusters at resolution 0.26. Subcluster 0-3 all express early migratory NCC program genes, but only subcluster 2 and 3 express a significant level of late migratory NCC program genes. (B) UMAP and re-clustering of the cranial NCC cluster into 21 smaller

1233 subclusters at a resolution of 2.0. (C-F) FeaturePlots show the expression of mesenchyme and
1234 neurogenic lineage markers in cranial NCC. Subcluster 2 displays a high expression of
1235 pharyngeal arch mesenchyme marker *Dlx2* (C). The frontonasal mesenchyme marker *Alx1* is
1236 specifically expressed by subcluster 3 (D). Neurogenic lineage markers *Nrp1* and *Nrp2* are
1237 expressed in late migratory NCC (E and F). (G-I) FeaturePlots showing expression of the
1238 premigratory NCC marker *Wnt1* (G) and neural plate border specifiers *Pax7 and Zic2* (H and I) in
1239 early migratory NCC. Subcluster 2' and 10' cells express reduced levels of *Wnt1*, *Zic2* and *Pax7*
1240 than subcluster 17' cells.

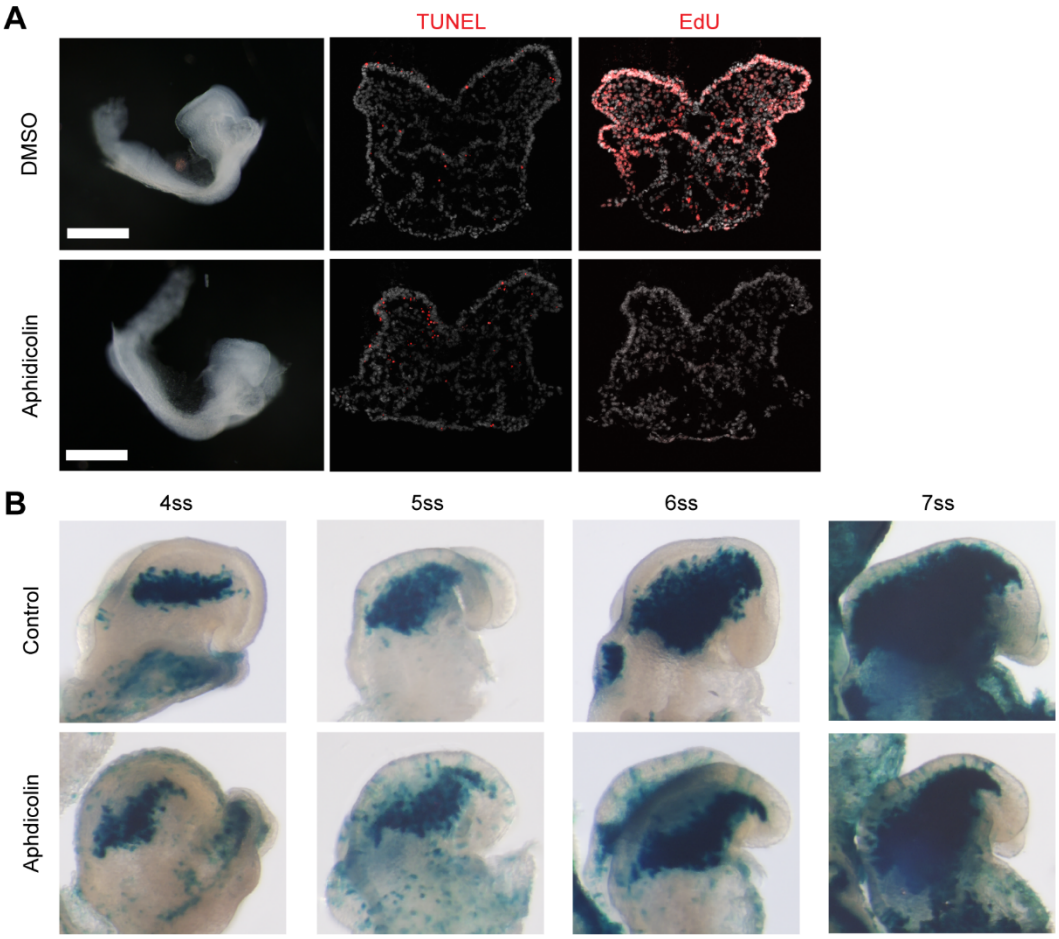

1241

1242 **Figure 4-figure supplement 1.** Aphidicolin treatment on *Mef2c-F10N-LacZ* embryos show
1243 consistent results as CD1 embryos. (A) Aphidicolin treatment in early E8.5 CD1 embryos for 12-
1244 13 hours prevented cells from entering S phase cell cycle and induced minimal cell death.
1245 Aphidicolin treated embryos exhibit a lack of EdU incorporation and a similar level of TUNEL
1246 signal compared to the control. (B) *Mef2c-F10N-LacZ* embryos treated with Aphidicolin for 12-
1247 13 hours exhibit reduced migratory NCC as evidenced by β-galactosidase staining.

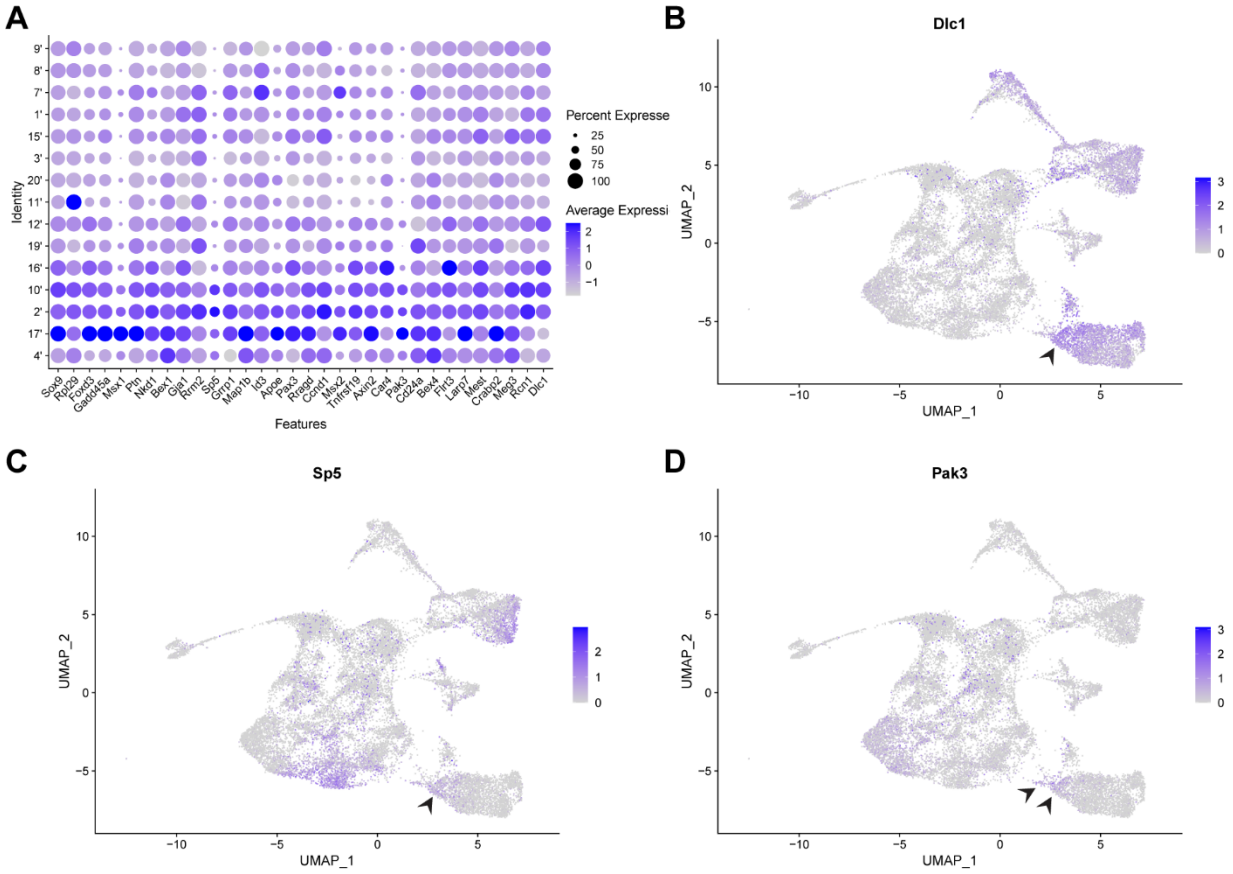

Figure 5-figure supplement 1. Expression of EMT intermediate NCC markers in scRNA-seq data. (A) Dotplot showing the expression of all EMT intermediate NCC markers in early migratory NCC subclusters (resolution 2.0). (B-D) FeaturePlots showing the expression of *Dlc1*, *Sp5* and *Pak3* in all early E8.5 cranial mouse embryo tissues. The expression of *Dlc1*, *Sp5* and *Pak3* is largely restricted to NCC, neuroectoderm and mesoderm cells. Arrowheads indicate *Dlc1*, *Sp5* and *Pak3* expression specifically in premigratory and intermediate NCC.

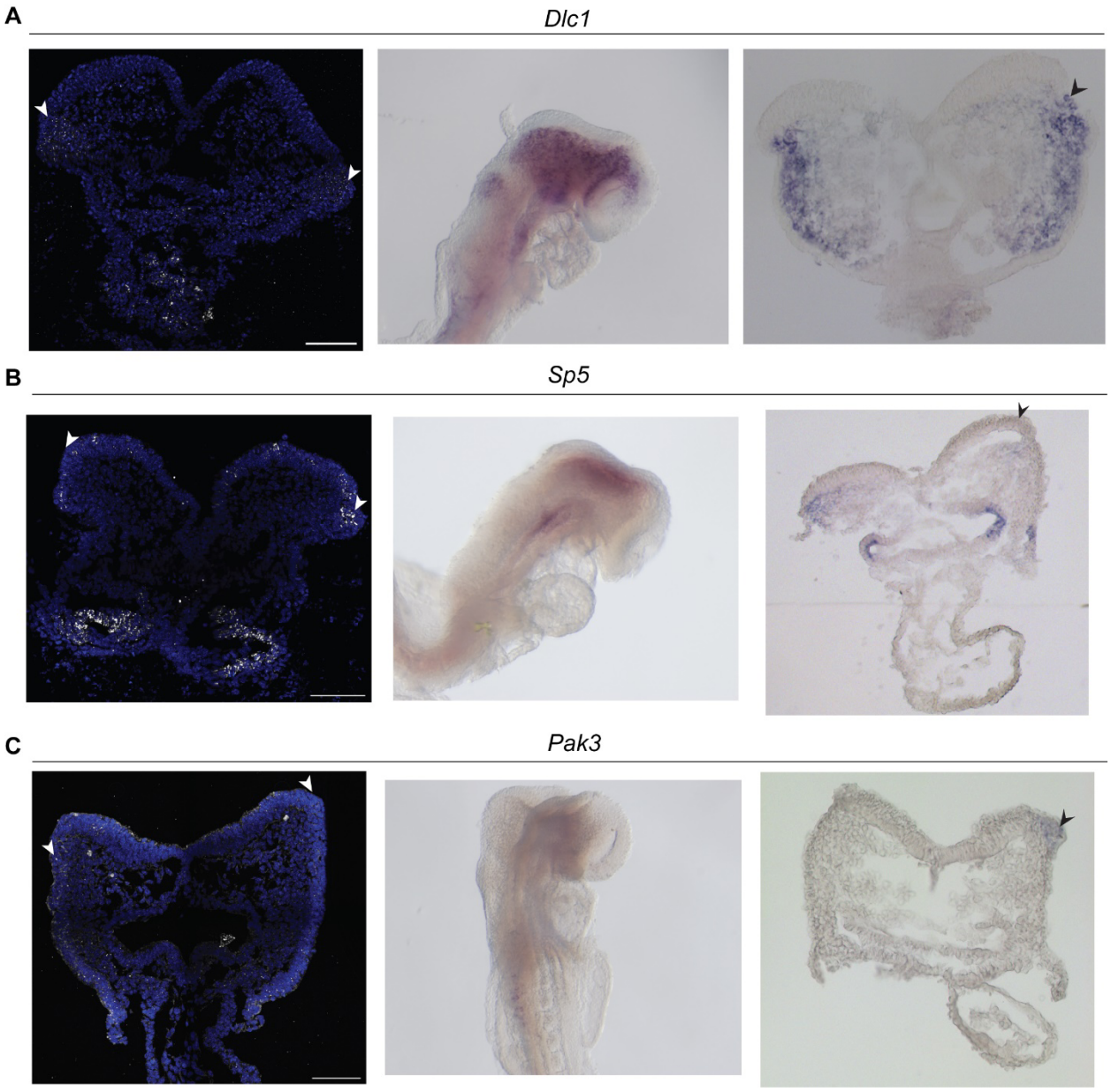

Figure 5-figure supplement 2. Expression of intermediate NCC markers *Dlc1*, *Sp5* and *Pak3* by SABER-FISH and traditional in situ hybridization in E8.5 mouse embryos and cranial sections. Arrowheads indicate positive signals in the dorsolateral neuroepithelium. (A) *Dlc1* signal was observed in the dorsolateral region of the neuroepithelium as well as in cells just outside of the neuroepithelium in the underlying mesenchyme. (B) *Sp5* expression is localized within the neuroepithelium and underlying dorsal mesenchyme. (C) *Pak3* expression is observed is ectodermal tissues including the neuroectoderm or neuroepithelium.

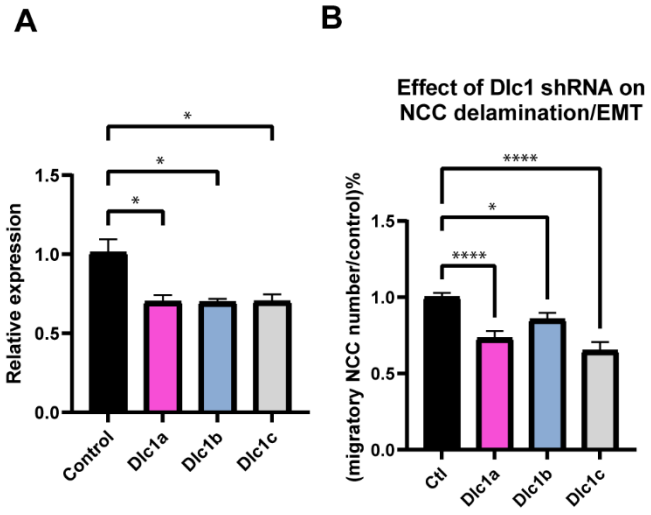

Figure 6-figure supplement 1. *Dlc1* plays a regulatory role in mouse cranial NCC EMT and delamination. (A) *Dlc1a*, *Dlc1b* and *Dlc1c* shRNA-based lentiviruses consistently achieved 30% reduction of *Dlc1* expression based on qRT-PCR analysis. *p<0.05. (B) Embryos injected with *Dlc1a*, *Dlc1b* and *Dlc1c* shRNA-based lentiviruses consistently showed significantly fewer migratory NCC compared to the control. The number of Sox10+ migratory NCC was quantified in control (n=4), *Dlc1a* (n=4), *Dlc1b* (n=4) and *Dlc1c* (n=4) embryos. All datapoints in *Dlc1a*, *Dlc1b* and *Dlc1c* samples were normalized to the control samples. *p<0.05. ****p<0.0001.

Supplementary Table 1. NCC development related genes.

Gene	Expression pattern in relation to NCC development	References
Sox2	Neural epithelium (reduced in neural plate border)	Hafemeister & Satija, 2019; Lee et al., 2013; Wood & Episkopou, 1999
Sox1	Neural epithelium (reduced in neural plate border)	Hafemeister & Satija, 2019; Lee et al., 2013; Wood & Episkopou, 1999
Zic1/2	Neuroepithelium	Sauka-Spengler & Bronner-Fraser, 2008
Wnt1	Neural plate border	Echelard et al., 1994; Parr et al., 1993
Pax7	Neural plate border	Murdoch et al., 2012
GCNF (Nr6a1)	Neural epithelium and early MNCC	
Zeb2	Neural epithelium and early MNCC	Van de Putte et al., 2003
Pax3	Neural plate border and early MNCC	Li et al., 2000
(Wnt1-Cre) EYFP	Neural plate border and early MNCC	Hari et al., 2012
Sox9	Neural plate border and early MNCC	Lee et al., 2013
Foxd3	Neural plate border and early MNCC	Dottori et al., 2001

Snail1	Neural plate border and early MNCC	Cheung et al., 2005
Mef2c-F10N-LacZ	Predominantly MNCC	Aoto et al., 2015
Vimentin	MNCC (marker of mesenchymal cells)	Kobayashi et al., 2020
Sox10	MNCC	Hari et al., 2012
Twist1	MNCC	Soo et al., 2002

1273

1274 Supplementary Table 2. Primers for qRT-PCR

	Forward (5'-3')	Reverse (5'-3')
Dlc1	AGCGGCTGTGAAAGAAA	GCATTACCCTTGGAGAAGA
B2M	CACTGACCGGCCTGTATGC	GGTGGCGTGAGTATACTTGAATTTG
CANX	CCAGACCCTGATGCAGAGAAG	CCTCCCATTCTCCGTCCATA

1275

1276

1277